Synthesis and Characterization of 1D CdS@Vanadium Doped ZnO Nanorods Arrays for Superior Interface Stability and Photoactivity to Produce Hydrogen

By

Omaima Amjad

Reg No. 0000365120

This thesis is submitted as partial fulfillment of requirements for the degree of

Master of Science

In

Chemistry

Supervisor: Dr Inayat Ali Khan

Co-supervisor: Dr Syed Shoab Ahmad Shah

Department of Chemistry, School of Natural Sciences

National University of Sciences and Technology (NUST),
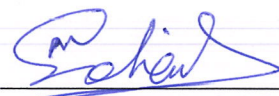
H-12 Islamabad, Pakistan

2024

THESIS ACCEPTANCE CERTIFICATE

Certified that final copy of MS thesis written by **Omaima Amjad** (Registration No **00000365120)**, of **School of Natural Sciences** has been vetted by undersigned, found complete in all respects as per NUST statutes/regulations, is free of plagiarism, errors, and mistakes and is accepted as partial fulfillment for award of MS/M.Phil degree. It is further certified that necessary amendments as pointed out by GEC members and external examiner of the scholar have also been incorporated in the said thesis.
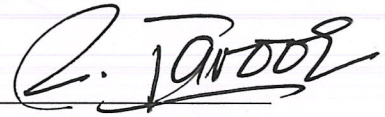
Signature: _____

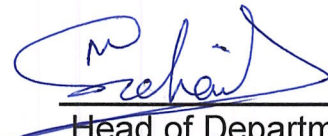Name of Supervisor: Dr. Inayat Ali Khan_____

Date: _____20|12|24_____

Signature (HoD): _____

Date: __23/12/2024_____

Signature (Dean/Principal): _____

Date: ___26·12·2024_____

National University of Sciences & Technology

MS THESIS WORK

We hereby recommend that the dissertation prepared under our supervision by: Omaima Amjad, Regn No. 00000365120 Titled Synthesis and Characterizations of 1D CdS@Vanadium Doped ZnO Nanorods Arrays for Superior Interface Stability and Photoactivity to Produce Hydrogen be Accepted in partial fulfillment of the requirements for the award of MS degree.

Examination Committee Members

1. Name: PROF. MANZAR SOHAIL   Signature: _____

2. Name: DR. KHADIJA MUNAWAR   Signature: _____

Supervisor's Name DR. INAYAT ALI KHAN   Signature: _____

Co-Supervisor's Name DR. SYED SHOAIB AHMAD SHAH   Signature: _____

_____
Head of Department

20/12/2024
Date

COUNTERSINGED

Date: 23.12.2024

_____
Dean/Principal

Abstract

A novel photoactive core-shell CdS@V doped ZnO nanorod (NR) heterostructure was successfully synthesized using hydrothermal and SILAR techniques. The crystallographic structures, phases, and compositions of all photoanodes were characterized by X-ray diffraction (XRD) and energy dispersive X-ray spectroscopy (EDX). Scanning electron microscopy (SEM) was used to examine the morphology and confirm the core-shell structure of the photoanodes. A novel core shell CdS@vdoped ZnO NRs heterostructure was synthesized and characterized successfully for photoelectrochemical hydrogen production. 8 cycled CdS was optimized on NRs with photocurrent density values 0.06 mA/cm^2. It shows the lowest charge transfer resistance, band gap values and the highest photoconversion efficiency values. After doping with V ions, the photocurrents density values and photoconversion efficiency values started to increase and charge transfer resistance goes to decrease. The photocatalyst CdS@vdoped ZnO NRs shows the highest photocurrent density values 0.51 mA/cm^2 and the lowest charge transfer resistance values 5.724 kΩ in the light. It shows the highest photoconversion efficiency value 0.24% vs RHE. This shows the successful type-II heterojunction formation which increase the charge carrier transfer and reduces the charge recombination by making Schottky barrier between them.

Contents

Table of Figure

Chapter 1

Introduction

1. Energy and its reserves

Energy is a crucial property generated through work, often appearing as heat or light, and can be converted from one form to another. Our heavy dependence on energy, particularly from fossil fuels, raises concerns about its potential depletion. Currently, over 80% of the world's energy comes from fossil fuels, which contribute significantly to environmental pollution. To mitigate these issues, adopting renewable energy sources is essential [1]. Options such as wind, hydropower, solar energy, and biomass offer sustainable alternatives. Among these, solar energy captured from sunlight emerges as the most effective and reliable source. This has been clearly demonstrated in countries like Turkey, where solar power has proven to be a leading energy solution. Countries like the UK and the USA develop strategies to address energy depletion and enhance the quality of life. Meanwhile, China generated approximately 10,065 metric tons of energy from fossil fuels, contributing to significant CO_2 emissions [2].
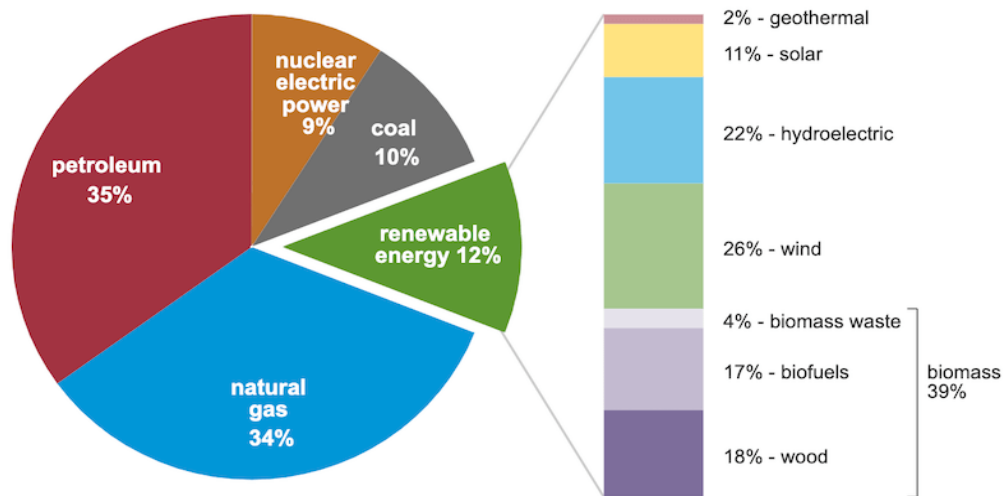

Figure 1 Percentage production of energy through different renewable sources

1.1. Types of Non-renewable Energy Reserves:

1.1.1. Coal Energy Reserve:

Coal plays a vital role in global electricity production. In 2001, around 38% of the world's electricity was generated from coal, equating to nearly one-third of the total energy output. By

2003, this figure increased slightly to 39%, a level that remained steady for several years. Although Turkey lacks abundant natural energy resources, it does have reserves of approximately 1.3 billion tons of hard coal and 8.058 billion tons of lignite. However, 99% of Turkey's lignite has a caloric value below 4000 kcal/g, making it lower in quality. This type of lignite is predominantly used in power plants for electricity production [3, 4].
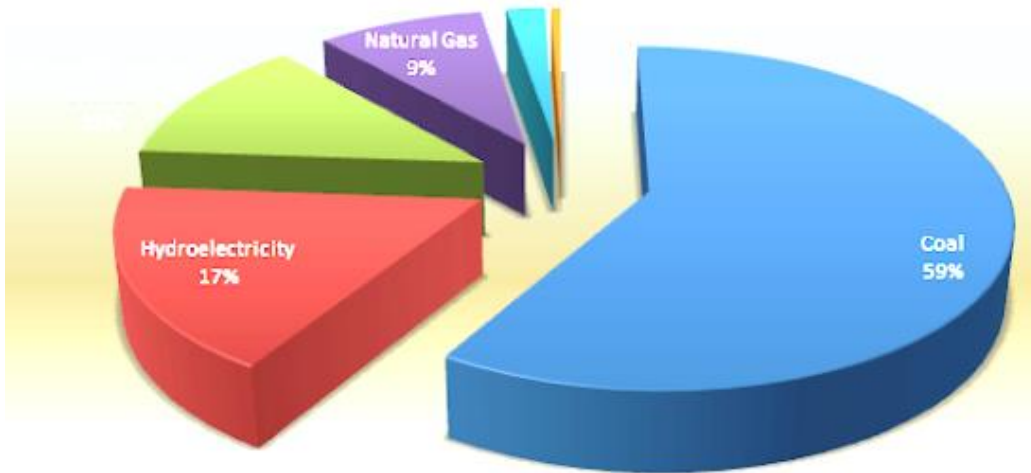
Figure 2 : Energy Production through coal consumption

1.1.2. Natural Gas Energy Reserve:

Natural gas hydrates release natural gas under standard temperature and pressure, producing double the carbon emissions compared to fossil fuels. They serve as an alternative energy source, primarily found in seafloor regions. These hydrates are transformed into natural gas when the necessary equilibrium conditions are met within hydrate reservoirs, requiring low temperatures and high pressures for extraction. Natural gas forms through two processes: thermo genic and biogenic. Thermo genic natural gas results from the decomposition of organic fossil fuels, such as hydrocarbons like methane, ethane, and propane. In contrast, biogenic natural gas is produced by methanogens and consists mainly of pure methane [5].

The data was analyzed to assess the impact of energy resource consumption on the green economy, covering the period from 1975 to 2018 across the top 10 countries worldwide. During this era of rapid economic expansion, environmental sustainability has become a significant challenge. The swift growth of the economy often leads to environmental harm due to the irresponsible use of

energy resources, which emit CO2 and contribute to global warming. In China, the sale of environmental safety assets has led to increased greenhouse gas emissions in nearly 30 of its regions. Notably, four areas, including Gansu province, are particularly linked to CO2 production due to their use of these resources. The distribution of unconventional energy resource usage is as follows: North America accounts for 34%, Asia-Pacific for 23%, South America for 14%, and Russia for 13% [6].
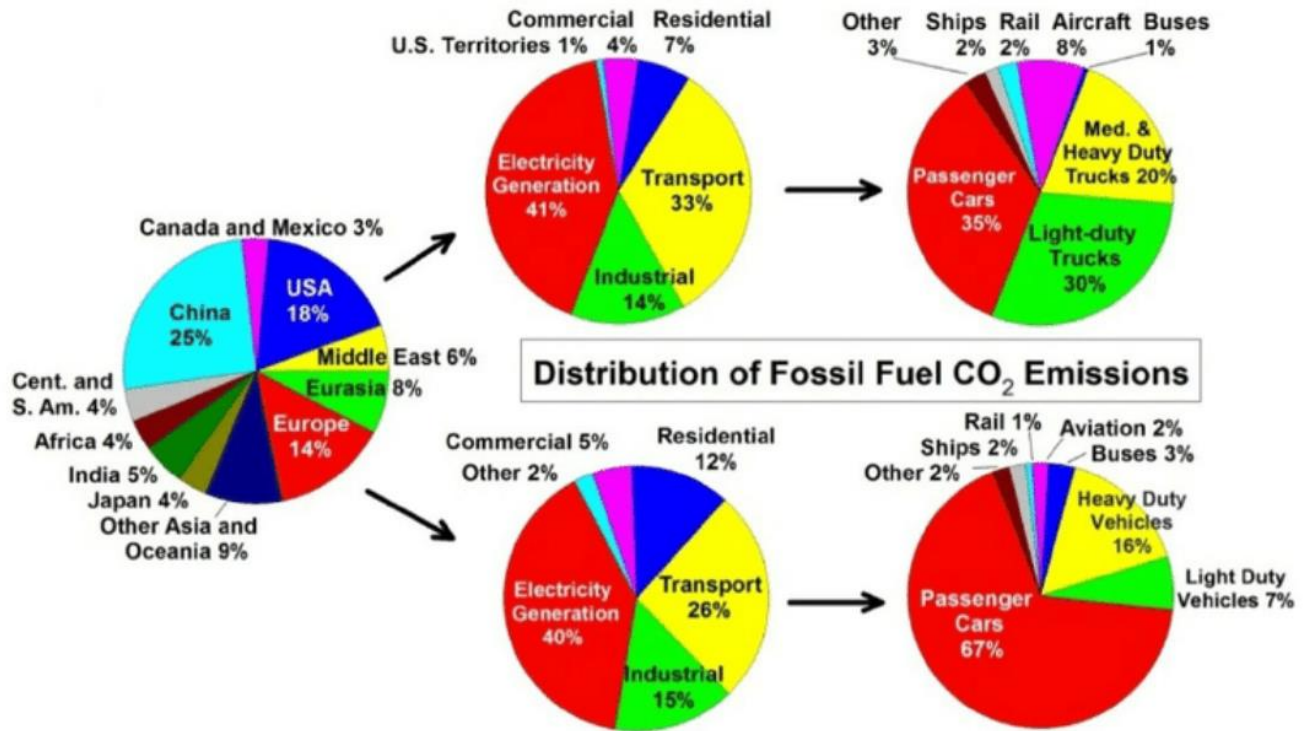
Figure 3 : Energy distribution by fossil fuel

1.2. Renewable Energy Reserves

1.2.1. Wind turbine installations

Wind power is regarded as one of the most competitive and effective energy sources because it addresses the issue of greenhouse gas emissions and helps mitigate global warming. Recently, countries such as China, India, the USA, Europe, and Brazil have been making significant efforts to reduce their reliance on fossil fuels and invest in renewable energy sources [7]. According to the International Energy Agency, wind power is expected to contribute up to 18% of clean energy production by 2050. Wind power generation is categorized into three timeframes: short-term

forecasts are used for predicting load fluctuations, medium-term forecasts support electricity market planning, and long-term forecasts help assess power systems and estimate electricity generation from wind power plants [8, 9].
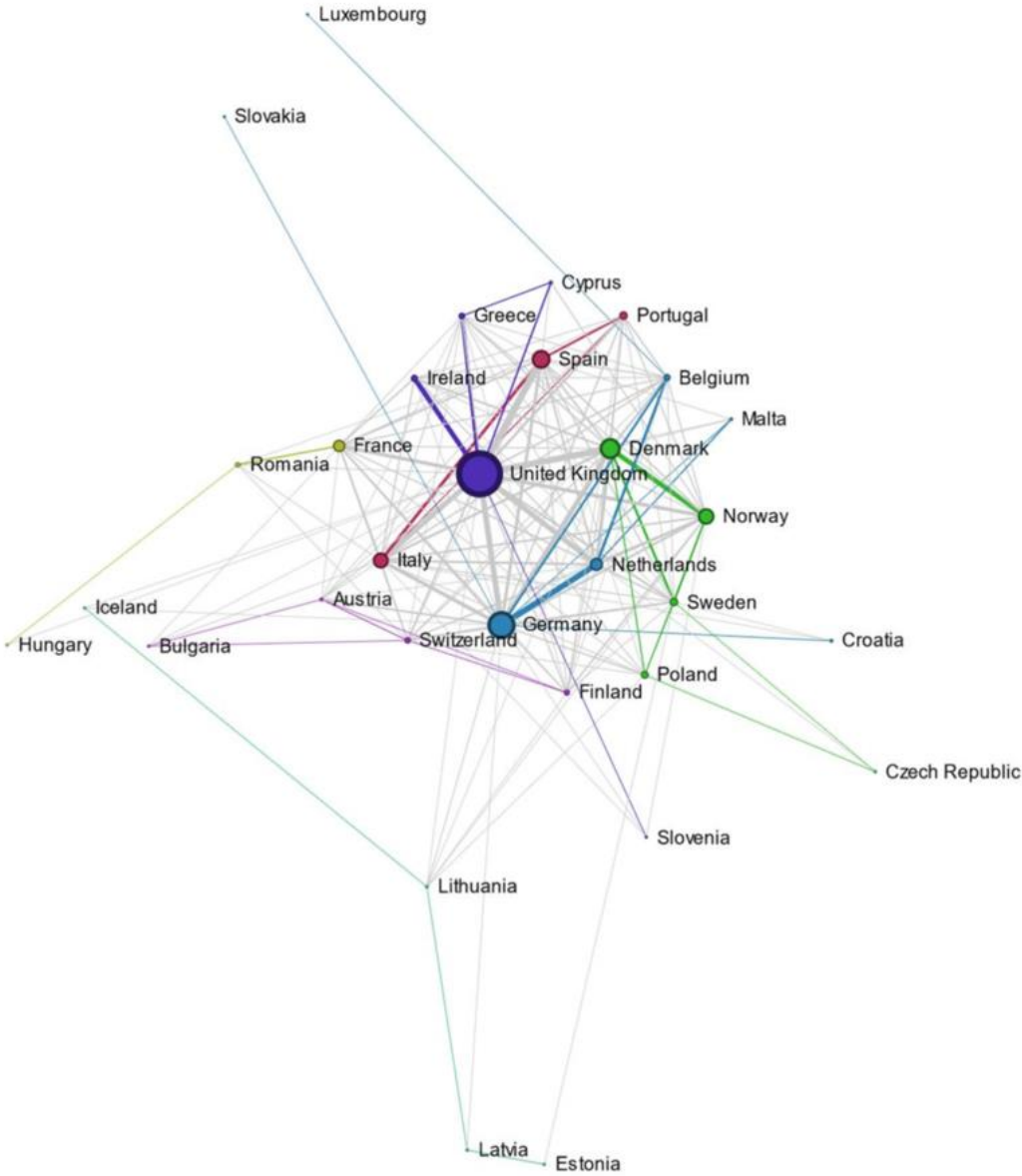
*Figure 4 : **countries' collaboration network for power generation through wind***

1.2.2. Water-based energy resources

Electricity is a crucial part of modern life, and hydropower resources are among the primary means of generating electricity using gravitational water vortex turbines. These systems are often

categorized as small hydropower systems, typically with a head of 1-2 meters and power outputs ranging from 100 W to 20 kW, with flow rates between 0.1 and 2 m³/s. Hydropower is particularly sensitive to environmental changes, especially variations in precipitation. In India, there are seven major hydropower plants that generate 25% of the country's electricity, significantly influencing water-based power generation [11].
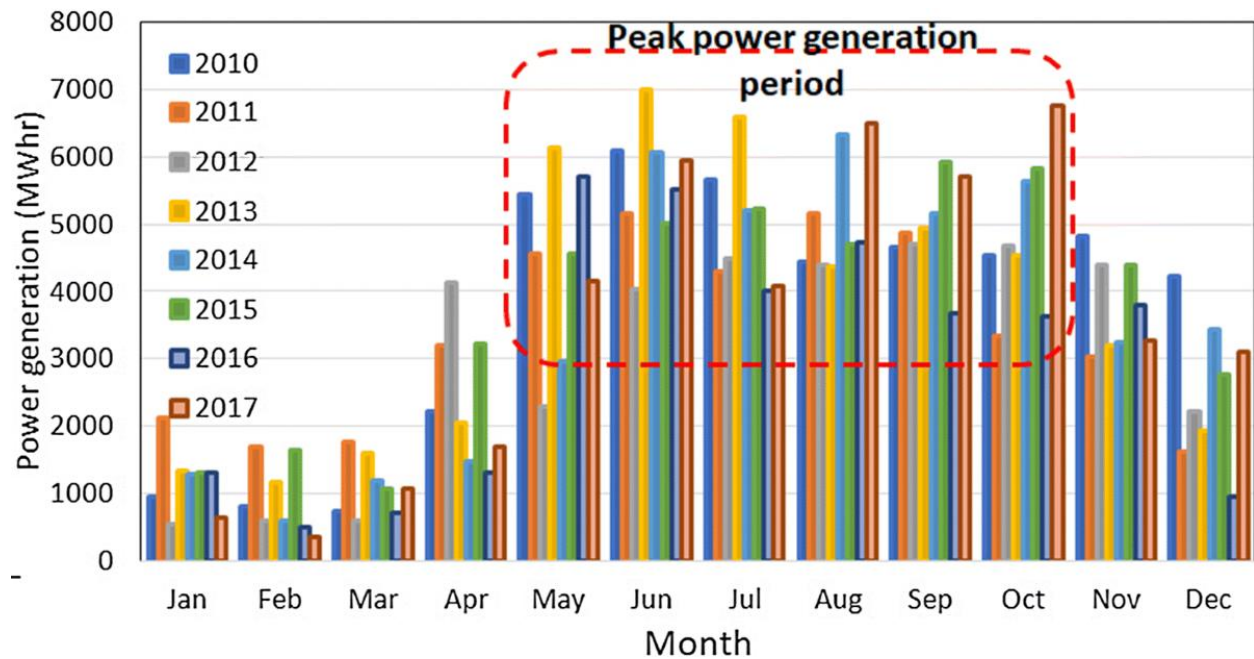
Figure 5: Hydropower generation and precipitation

1.2.3. Solar energy supplies

The demand for solar energy is steadily increasing due to population growth and advancements in technology. Among all renewable energy sources, solar energy stands out as the most promising, reliable, and freely available resource to address the energy crisis. In many countries, especially developing nations, solar energy is essential for meeting energy needs. For instance, Sri Lanka receives an average solar radiation of about 15-20 MJ/m²/day [12]. One of the key benefits of using solar energy is that it does not harm the ecosystem, allowing natural systems to stay balanced and supporting the well-being of all living organisms. Recent advancements in technology have enabled the conversion of solar energy directly into chemical energy and electricity through methods such as concentrating solar thermal power (CSP) and concentrating photovoltaic technology (CVT) [13]. These technologies can convert up to 90% of solar energy into usable power. The highly developed photovoltaic cells used in these systems can function at 100%

capacity for up to 10 years and at 80% capacity for up to 25 years. However, the efficiency of photovoltaic cells is dependent on sunlight intensity. Every year, the Earth receives about four million extra joules of solar energy, a vast amount that remains largely untapped for energy production. In the USA, solar power plants supply energy to about 113,533 homes and help reduce greenhouse gas emissions. The main drawback of solar energy systems is that they generate electricity only during the day, as solar energy is unavailable at night. However, solar energy storage systems have been developed to store energy, allowing it to be used at night for electricity production [14].
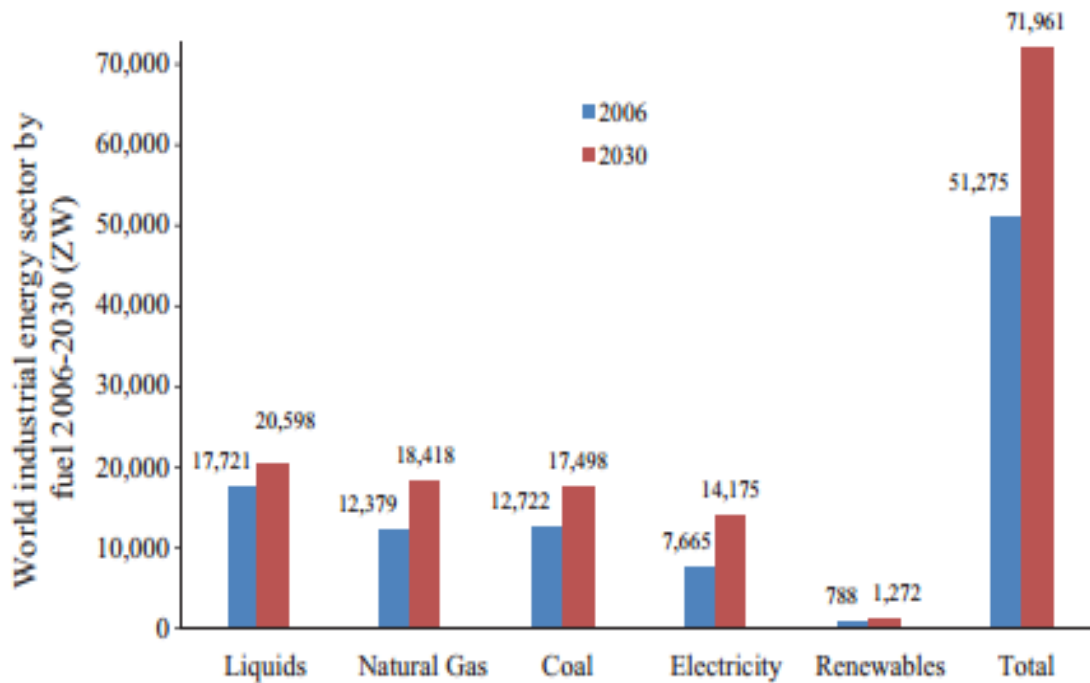
Figure 6 : World Industrial Sectors

1.2.4. Organic energy resources

Biomass is a renewable energy resource with significant potential to meet energy needs, particularly in the form of wood. It ranks as the fourth-largest energy source, fulfilling 14% of global energy demand. Biomass is unique in that it contains a fixed amount of carbon and provides more energy than many other energy sources. In industry, about 3% of biomass energy is utilized. In rural areas, approximately 50% of the global population relies on biomass as an energy source. Worldwide, total energy production amounts to 2740 quads. In the 1970s, the US energy

consumption from biomass was equivalent to 850,000 barrels, which increased to 1.4 million barrels per day by the 1990s [15]. Biomass energy is primarily used for electricity generation and in the wood and paper industries. Biomass can be used both directly and indirectly. Direct use includes burning wood for heating and cooking in homes, while indirect use involves converting substances like sugarcane juice or animal waste into gas. The energy produced by biomass combustion is around 8 MJ/kg for wood, 20 MJ/kg for plants, and 55 MJ/kg for methane. To generate electricity from biomass, steam power plants are used, where a two-fluid system transfers energy between water and combustion gases. In the US, biomass power plants generated 200 MW in 1979, and this capacity increased to over 6000 MW by the 1990s [16].

Figure 7: Biomass Electricity Production

1.2.5. Photo-catalyst

Photocatalysts are highly effective materials for addressing energy and environmental challenges. They are generally classified into two main categories. The first category includes metal-based photocatalysts, such as metal oxides, metal sulfides, metal nitrides, and metal phosphates, as well as metal-free photocatalysts like C3N4 [17]. The second category consists of metals that exhibit the localized surface plasmonic resonance (LSPR) effect, such as silver (Ag), gold (Au), and

7

platinum (Pt). Metal-based photocatalysts can operate through either direct or indirect electron transition methods and are used for applications such as water splitting, CO2 reduction, waste treatment, and N2 reduction. LSPR photocatalysts generate hot electrons on particles of Au, Ag, and Pt, which are used in processes like water splitting and waste treatment [18].
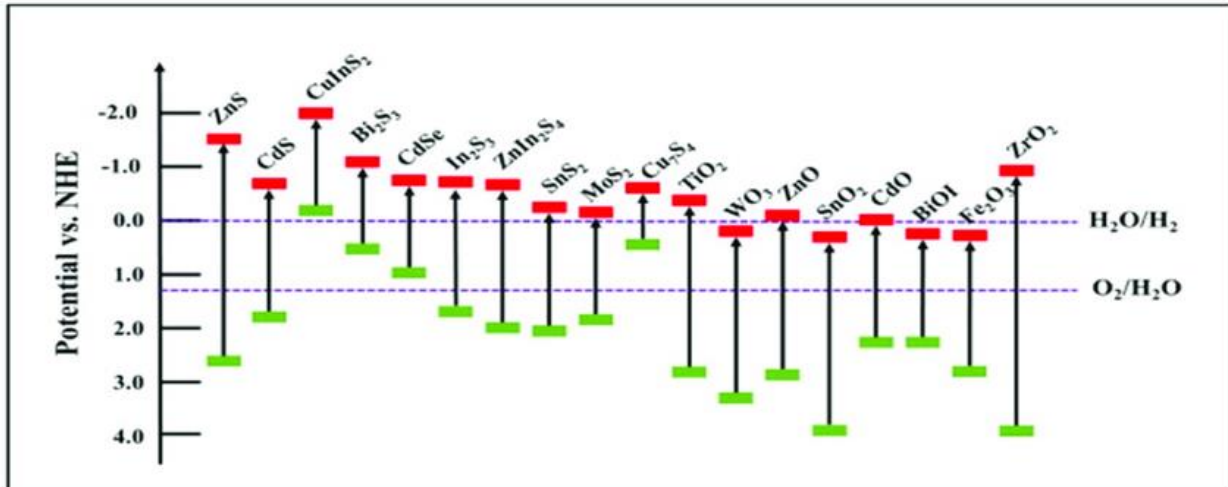
Figure 8: Metal oxides and their band gap

1.2.6. n-type Semiconductor

The n-type semiconductors possess distinct electronic configuration properties. In these semiconductors, oxygen vacancies are created in sufficient quantity to supply electrons, providing a pathway for electron transport within the conduction band, which is typically composed of s orbitals. These s orbitals are spread out, resulting in significant electron hybridization, even in the material's amorphous state [19]. These semiconductors feature delocalized conduction band maxima, which help reduce the effective electron mass, enhance charge mobility, and improve
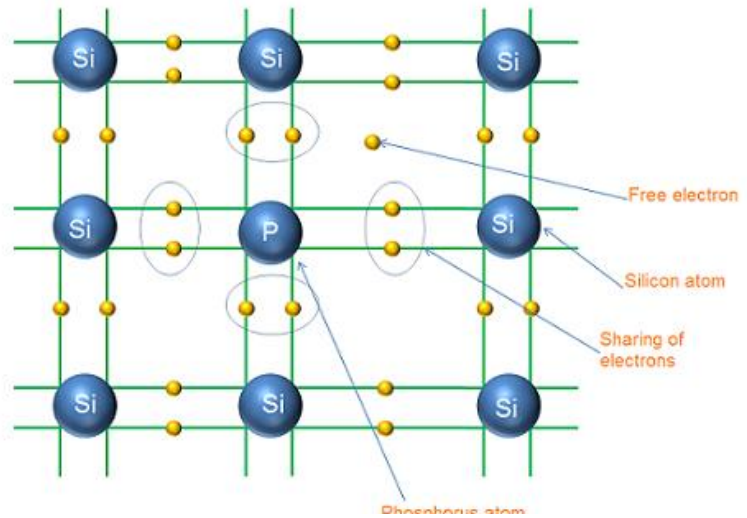
Figure 9: n-type Semiconductor

charge transport. N-type semiconductors exhibit a positive slope in Mott-Schottky plots and have a Fermi level positioned below the conduction band of the material [20].

1.2.7. p-type Semiconductor

p-type semiconductors are those in which the Mott-Schottky plots display a negative slope, and the Fermi level is located above the valence band. These semiconductors are typically doped with electron acceptor atoms, making them extrinsic semiconductors [20].
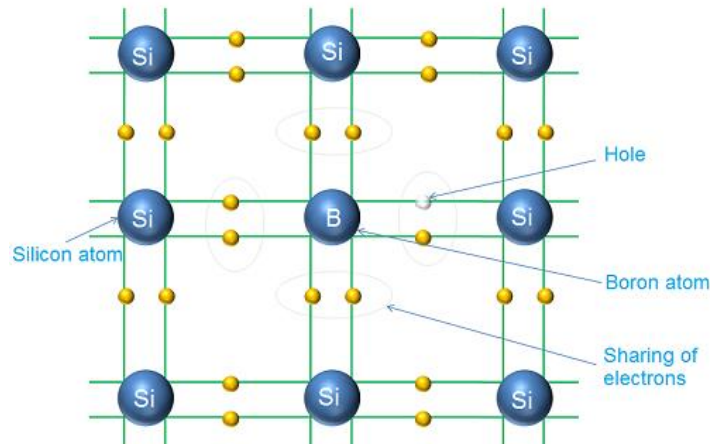
Figure 10: p type Semiconductor

1.3. Hetero junction Formation

The creation of a hetero junction involves six main steps

1. The semiconductor initially absorbs light from the sun.

2. Electrons and holes are generated as a result.

3. Electrons and hole pairs migrate toward their corresponding conduction and valence bands.

4. Reactants are adsorbed onto the active sites of the photo catalysts.

5. Once the products are formed, they are desorbed.

6. Redox reactions take place on the semiconductor's surface [21].

1.3.1. Types of Heterojunctions

There are several types of heterojunctions, one of which is the Type-II heterojunction, also known as the staggered gap. In this type of heterojunction, consider two semiconductors, A and B. The conduction band of semiconductor A is positioned higher than that of semiconductor B, while the

valence band of semiconductor B is higher than that of semiconductor A. When exposed to light, both semiconductors absorb photons, and the electrons generated by light absorption migrate to their respective conduction bands, leaving behind holes. The movement of charge carriers generates an internal electric field. The electrons move from the more negative conduction band to the less negative conduction band, causing reduction, while the holes move in the opposite direction, leading to oxidation on the semiconductor [22].

1.3.2. **Direct Z-Scheme Heterojunction:**

A Direct Z-Scheme Heterojunction is similar to the indirect Z-scheme, but without the use of an electron mediator. In this scheme, electrons and holes are separated at higher reduction and oxidation potentials. The charge transfer in this setup is more efficient than in a Type-II heterojunction due to the electrostatic interactions between the electrons and holes. Consider two semiconductors, A and B. After the electrons from both semiconductors migrate to their respective conduction bands, leaving behind holes in the valence bands, an electrostatic attraction is established between the two semiconductors. This attraction enables the electrons from the lower conduction band to recombine with the holes in the higher valence band. At the same time, electrons from the higher conduction band participate in reduction at higher reduction potentials, while holes from the lower valence band facilitate oxidation at higher oxidation potentials [22].
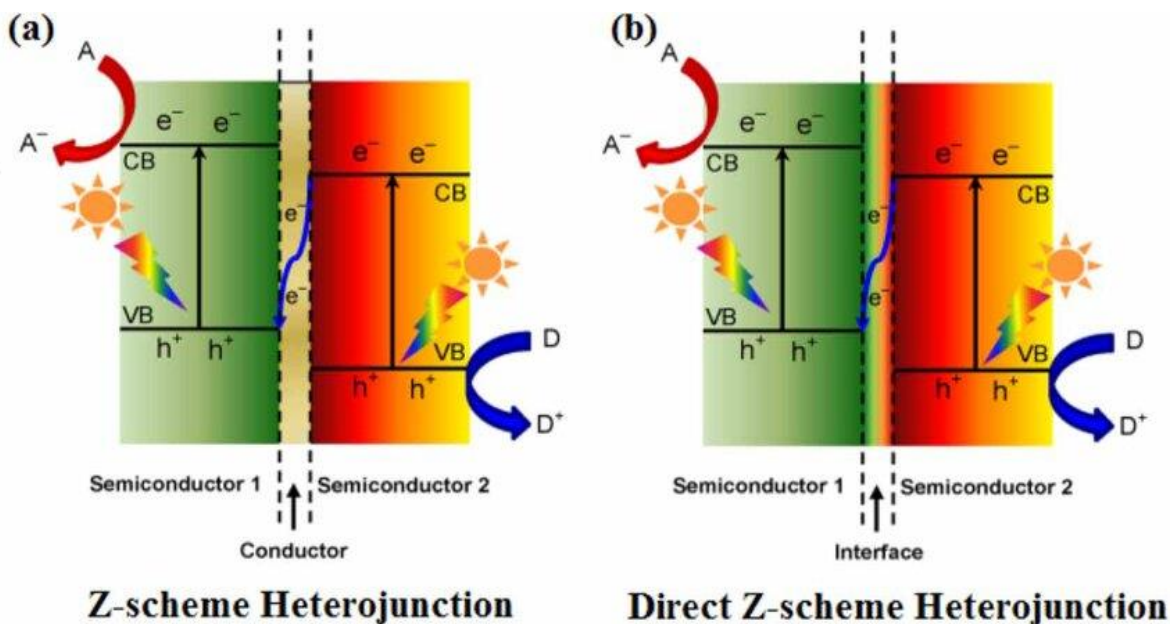

Figure 11: *Direct Z-Scheme Heterojunction*

1.4. Indirect Z-Scheme Heterojunction

An Indirect Z-Scheme Heterojunction involves the use of electron mediators, such as Au, Ag, or Pt, between two semiconductors to facilitate the transfer of charge carriers. Upon excitation, the electrons from both semiconductors migrate to their respective conduction bands, and the holes move to the valence bands. The electron mediator regulates the movement of electrons from the lower conduction band and holes from the higher valence bands. Meanwhile, electrons in the higher conduction band and holes in the lower valence band participate in reduction and oxidation processes at their respective higher reduction and oxidation potentials [23].
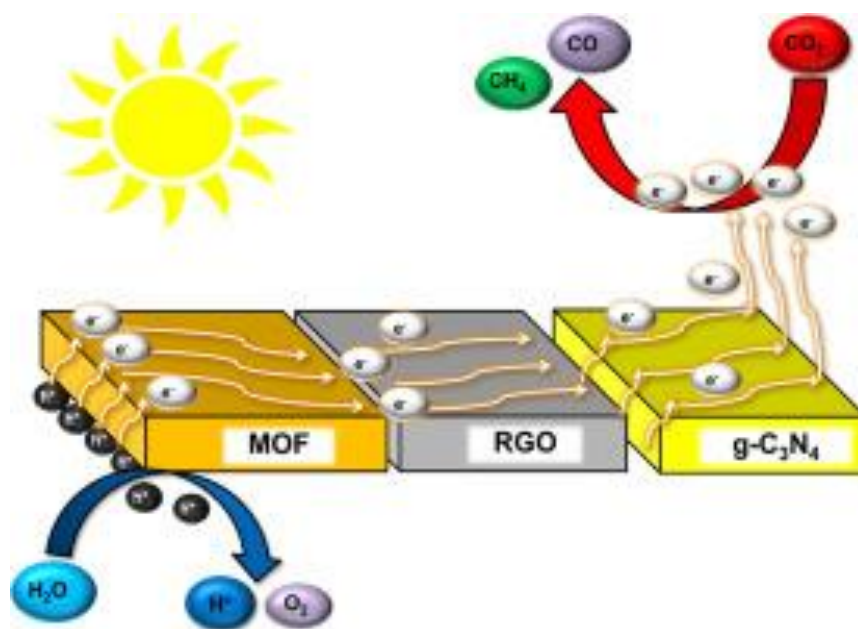
Figure 12: Indirect Z-Scheme Heterojunction

1.5. Step-Scheme Heterojunction:

A Step-Scheme Heterojunction involves two semiconductors, with one acting as the reduction photocatalyst (RP) and the other as the oxidation photocatalyst (OP). The RP is responsible for reducing electrons, while the OP facilitates the oxidation of holes. When electrons migrate from the valence band to the conduction band, the movement of charge carriers generates an internal electric field, enabling electrons to transfer from one semiconductor to the other. The electrons in the OP are ineffective because this photocatalyst is involved in oxidation, and the holes in the RP cannot participate in the reaction. As a result, the electrons from the OP and the holes from the RP

recombine, while the electrons from the RP take part in reduction at higher reduction potentials, and the holes in the OP enable oxidation at higher oxidation potentials [23].
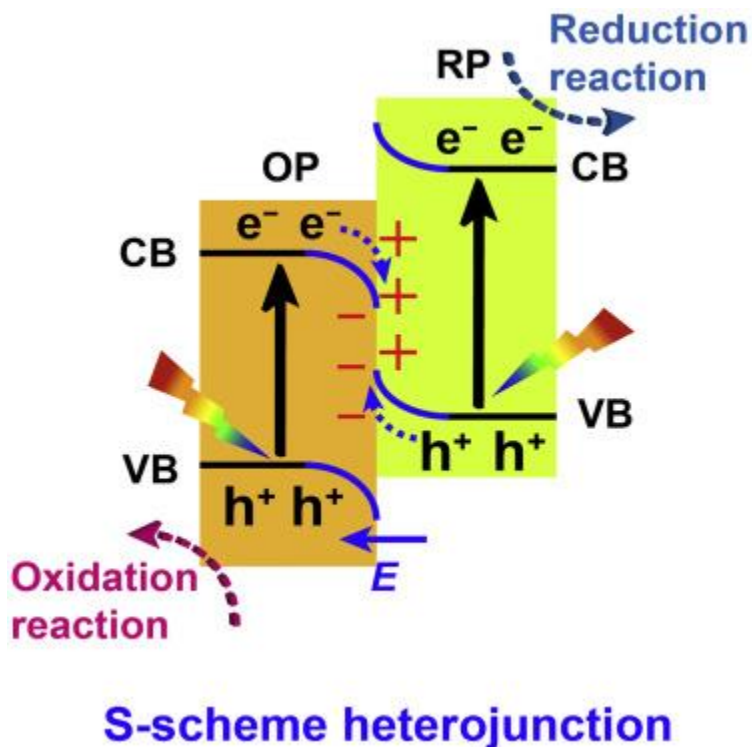
Figure 13: Step-Scheme Heterojunction

1.6. Doping in Semiconductors:

Doping in semiconductors refers to the introduction of impurities into the crystal lattice to enhance the material's physical and chemical properties. Doping can be achieved using either metal or non-metal elements. When metal is used for doping, extrinsic defects are created beneath the conduction band, which reduces the material's band gap, minimizes charge recombination, and enhances charge transfer. In contrast, doping with non-metals places the 2p orbital of the dopant above the semiconductor's valence band. This also reduces the band gap, facilitates the migration of electrons to the conduction band, and increases electron reduction. Doping with metals is referred to as n-type doping, while doping with non-metals is known as p-type doping [24].

1.7. Photoelectrochemical Water Splitting

Photoelectrochemical water splitting (PECWS) is an important and cost-effective method for hydrogen gas production. It was introduced by Fujishima and Honda using highly efficient and

low-cost semiconductor materials. The key principle of PECWS is the generation of hydrogen gas through solar light absorption, with an external bias voltage applied to a photoelectrode immersed in an electrolyte. In PEC water splitting, photon absorption initiates the reaction, generating electron-hole pairs. These charge carriers migrate to the surface of the photocatalyst and react at the active sites. The electrons move to the conduction band, while the holes move to the valence band. The electrons reduce hydrogen ions to form hydrogen gas at zero reduction potential, and the holes oxidize hydroxyl ions to oxygen at 1.23V oxidation potential. In nanomaterials, the reduced size, controlled shape, and morphology enhance charge carrier generation, leading to a 50-90% increase in the efficiency of PEC water splitting [25].
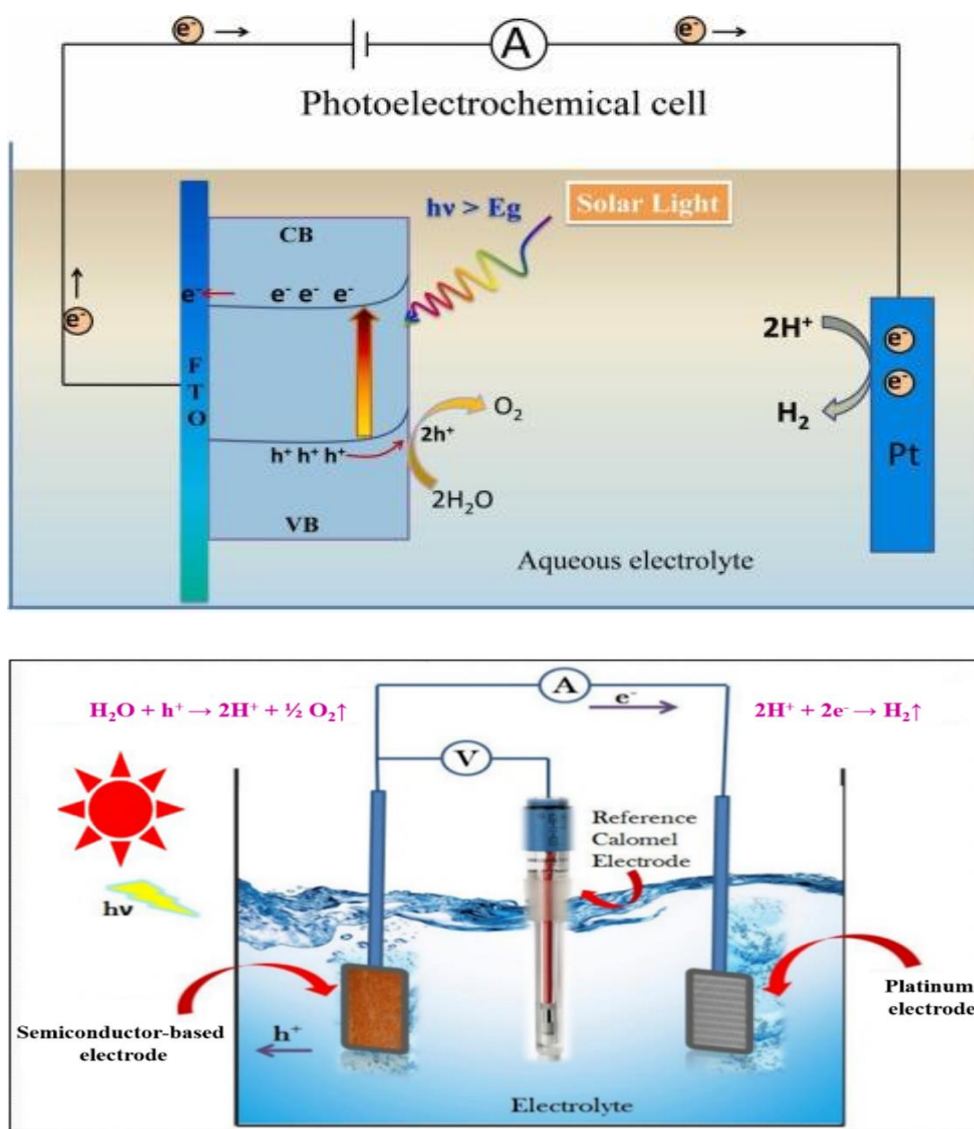

Figure 14: Photo electrochemical water splitting

<div align="center">**Chapter 2**</div>

2. **Literature Review**

Zinc oxide (ZnO) nanorods have attracted considerable interest due to their distinct structural, optical, and electronic characteristics, which make them ideal candidates for a wide range of applications, including sensors, optoelectronics, and energy devices. These nanorods are commonly synthesized through techniques such as hydrothermal, chemical vapor deposition, and sol-gel processes, each offering benefits in controlling their size, shape, and alignment. Research has shown that the high surface-to-volume ratio of ZnO nanorods boosts their photocatalytic performance, making them effective for environmental applications like wastewater treatment (Li et al., 2020).

Moreover, the piezoelectric properties have shown promise in energy harvesting systems (Zhu et al., 2019), while their wide bandgap (3.37 eV) facilitates efficient ultraviolet light emission, making them suitable for use in UV photodetectors and light-emitting diodes (LEDs)

Guo et al. showed recent progress in doping and functionalization techniques has further enhanced the capabilities of ZnO nanorods, emphasizing their versatility and potential for future technological advancements.

Zinc oxide (ZnO) nanorods have become a focal point of extensive research due to their exceptional properties and potential applications in areas like optoelectronics, photocatalysis, and energy harvesting. Their one-dimensional (1D) structure enhances electron mobility and provides a high surface-to-volume ratio, making them ideal for use in applications such as gas sensors, UV photodetectors, and piezoelectric devices (Zhang et al., 2018).

The methods used to grow these nanorods, including hydrothermal synthesis, chemical vapor deposition (CVD), and sol-gel processes, play a crucial role in determining their structural characteristics and functionalities. For example, hydrothermal synthesis allows for precise control over the nanorods' length and diameter, influencing their optical and electronic properties (Chen et al., 2020).

In photocatalysis, ZnO nanorods have been widely investigated for their ability to break down organic pollutants and remove harmful chemicals from wastewater, with their efficiency further improved through doping or functionalization with materials like silver or carbon-based substances (Liu et al., 2021).

Additionally, the piezoelectric properties of ZnO nanorods have been applied in energy harvesting systems, where they can convert mechanical energy into electricity, offering promising potential for sustainable energy production (Wang et al., 2019). These unique characteristics position ZnO nanorods as versatile candidates for future technologies, and ongoing research is focused on enhancing their performance through innovative synthesis techniques and composite materials.

Vanadium (V)-doped ZnO nanorods have gained attention as a promising material for various advanced applications due to the enhanced properties resulting from vanadium incorporation. Doping ZnO with V has been shown to improve its electronic, optical, and catalytic properties, making it suitable for use in sensors, photocatalysis, and energy conversion devices. Research has indicated that V doping creates mid-gap states within the ZnO band structure, improving charge carrier separation and boosting photocatalytic activity for organic pollutant degradation (Zhao et al., 2019).

Moreover, V-doped ZnO nanorods exhibit enhanced gas-sensing capabilities, showing increased sensitivity to gases like ethanol and NO2, thanks to improved electronic interactions at the ZnO surface (Sharma et al., 2020).

The synthesis methods, such as hydrothermal and sol-gel processes, significantly impact the size, shape, and uniformity of the nanorods, which in turn influence the performance of V-doped ZnO in various applications (Jiang et al., 2021). Additionally, the presence of V enhances the material's UV absorption and photoluminescence properties, making it a potential candidate for optoelectronic devices. Overall, the inclusion of vanadium in ZnO nanorods significantly improves their functionality, offering the potential for more efficient and sustainable technologies.

The synthesis of CdS-ZnO nanorods and their use in water splitting has been widely investigated, as the combination of CdS and ZnO significantly improves photocatalytic performance through their synergistic effects. CdS is known for its high efficiency in visible light absorption, while ZnO excels in electron transport. Several fabrication methods, such as hydrothermal, sol-gel, and

chemical vapor deposition, have been utilized to create CdS-ZnO nanorods, allowing precise control over their morphology, size, and structure, which are crucial for optimizing photocatalytic efficiency in water splitting (Zhao et al., 2021).

Additionally, doping or functionalizing these nanorods with other materials enhances their performance by promoting charge separation, minimizing recombination, and increasing surface area for better interaction with water molecules (Chen et al., 2020). In conclusion, CdS-ZnO nanorods hold great potential for water splitting, providing an effective approach for sustainable hydrogen production using solar energy.

Chapter 3

3. Experimental Section

3.1. Materials:

Zinc nitrate (ZnNO$_3$), hydrochloric acid (HCl 36-38% by weight), silver nitrate (AgNO$_3$), triethanolamine (TEA), hexamethylenetetramine (HMTA), Cadmium Sulphide (CdS), bismuth nitrate pentahydrate (Bi(NO$_3$)$_3$.5H$_2$O), vanadium pentoxide (V$_2$O$_5$), distilled water were obtained from Sigma Scientific (Pvt) ltd. All the chemicals were of analytical grade.

3.2. ZnO Seeding Process:

To prepare a uniform ZnO seed layer on fluorine-doped tin oxide (FTO) substrates, the substrates were first cleaned by immersing them in ethanol and deionized water, followed by sonication for 15 minutes, rinsing with DI water, and drying with nitrogen. A seeding solution was prepared by dissolving 164 mg of zinc acetate in 15 mL of ethanol; since the solution appeared cloudy, a few drops of triethanolamine (TEA) were added to stabilize and fully dissolve the zinc acetate, resulting in a clear solution. The solution was then spin-coated onto the cleaned FTO substrates using a syringe to dispense it at the center, with the spin coater set to 2000 rpm for 60 seconds. This process was repeated for six cycles, with a brief drying period between each cycle. After spin coating, the substrates were annealed in a furnace at 450°C for 3 hours to promote crystallization and improve adhesion, forming a uniform and adherent ZnO seed layer as the base for subsequent 1D ZnO nanorod growth.
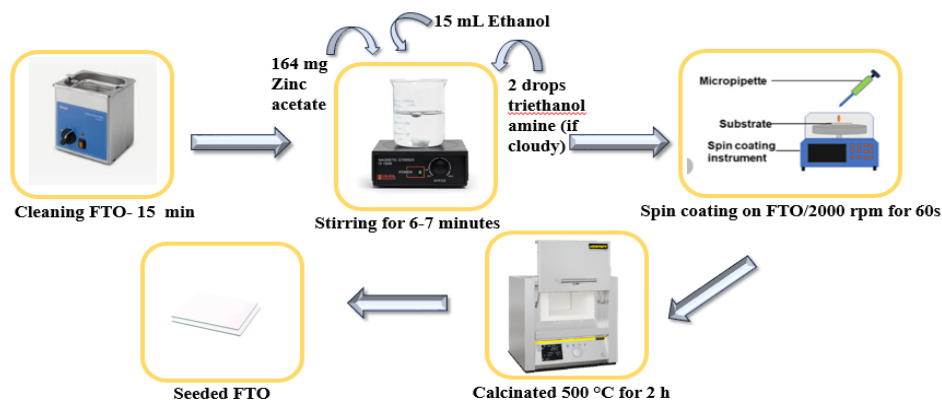

Figure 15: Seeding Process

3.3. Synthesis of 1D ZnO Nanorods:

1D ZnO nanorods were synthesized using a hydrothermal method. First, a 0.1 M solution of zinc nitrate was prepared by dissolving 446 mg of zinc nitrate in 15 mL of deionized (DI) water. Separately, a 0.1 M solution of hexamethylenetetramine (HMTA) was prepared by dissolving 210 mg of HMTA in 15 mL of DI water. The two solutions were mixed thoroughly for 60 seconds to form a homogeneous precursor solution. The cleaned FTO substrate, coated with the ZnO seed layer, was then placed in an autoclave in the correct upright position, ensuring that the conductive side faced the precursor solution. The autoclave was sealed and heated in an oven at 95°C for 12 hours to promote the hydrothermal growth of ZnO nanorods.

After the reaction, the FTO substrate was removed from the autoclave, rinsed thoroughly with DI water to remove any residual chemicals, and dried. Finally, the ZnO nanorods formed on the FTO substrate were annealed in a furnace at 450°C for 3 hours to enhance their crystallinity and stability. This process resulted in vertically aligned 1D ZnO nanorods.
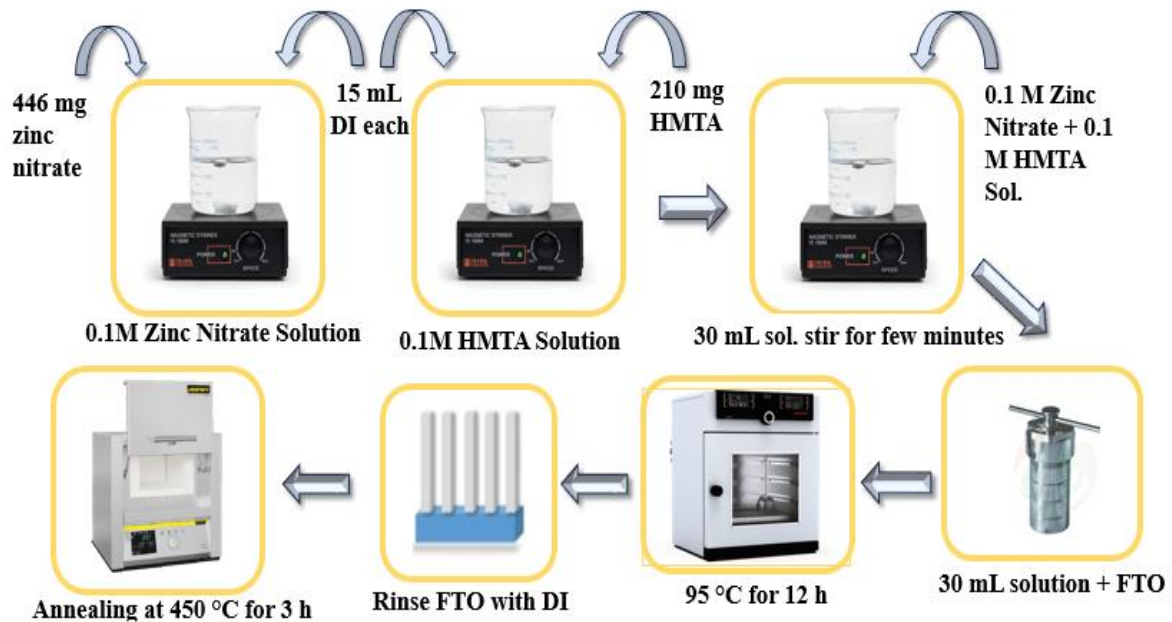

Figure 16: Synthesis of ZnO nanorods

3.4. Synthesis of CdS Layer on ZnO Nanorods by SILAR Technique

The CdS layer was deposited onto ZnO nanorods using the Successive Ionic Layer Adsorption and Reaction (SILAR) technique. A 0.01 M cadmium nitrate solution was prepared as the cationic

source, and a 0.01 M sodium sulfide (Na_2S) solution was prepared as the anionic source. The FTO substrate coated with ZnO nanorods was first immersed in the cadmium nitrate solution for 60 seconds, allowing cadmium ions to adsorb onto the surface of the ZnO nanorods. Afterward, the substrate was rinsed in deionized (DI) water to remove any excess ions. The substrate was then heated at 100°C for 2–3 minutes to stabilize the adsorbed cadmium layer.

Next, the FTO substrate was dipped into the sodium sulfide solution for 60 seconds to introduce sulfide ions, followed by another rinse in DI water. The process was repeated for the desired number of CdS layers (2, 4, 6, 8, and 10 layers), with the substrate being dipped alternately in the cadmium nitrate and sodium sulfide solutions. After each cycle, the substrate was rinsed with DI water and dried at 100°C.

Finally, to enhance the crystallinity and stability of the CdS layer, all the FTO substrates were annealed in an argon gas atmosphere at 400°C for 60 minutes. This process resulted in the formation of well-defined CdS layers on the ZnO nanorods, with the thickness of the CdS layer increasing with each successive deposition cycle.
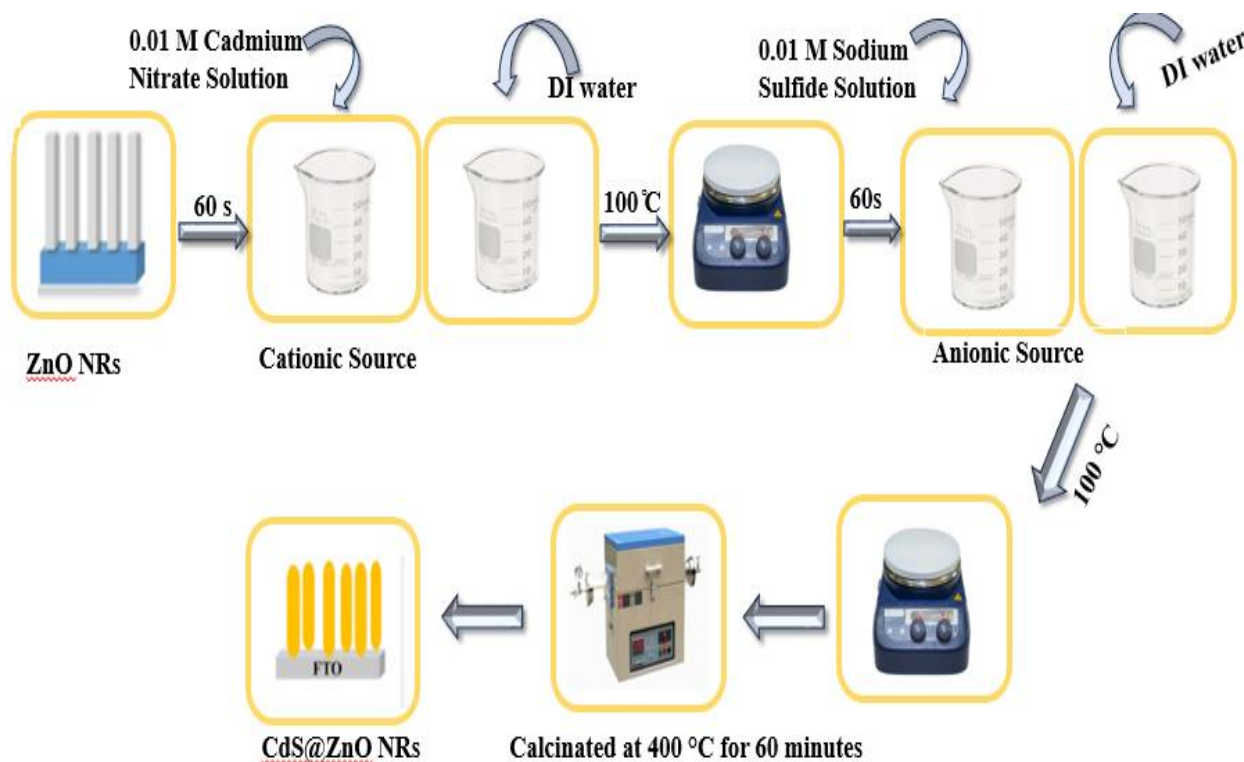

Figure 17: CdS Coating on ZnO nanorods

3.5. Hydrothermal Doping of Vanadium into ZnO Nanorods:

The hydrothermal doping of vanadium into ZnO nanorods was carried out by incorporating varying amounts of vanadium pentoxide (V_2O_5) into the synthesis solution. First, a 0.025 M solution of zinc nitrate was prepared by dissolving zinc nitrate in deionized (DI) water, and a 0.025 M hexamethylenetetramine (HMTA) solution was also prepared. Both solutions were stirred at 60°C for 30 minutes to ensure complete dissolution. Next, a specific amount of vanadium pentoxide (V_2O_5) was added to the solution to achieve doping concentrations of 2%, 4%, and 6% by weight. The solution was then stirred at 60°C for an additional 30 minutes to ensure thorough mixing and uniform distribution of the vanadium.

The prepared solution was transferred to an autoclave along with the seeded FTO substrate. The autoclave was sealed and heated at 95°C for 12 hours, allowing the hydrothermal growth and doping of the ZnO nanorods with vanadium. After the reaction, the FTO substrates were removed from the autoclave, rinsed thoroughly with DI water to remove any residual solution, and dried.

Finally, the FTO substrates were annealed at 450°C for 3 hours to enhance the crystallinity and stability of the doped ZnO nanorods. This process was repeated with different vanadium concentrations of 4% and 6% by weight of V_2O_5 to investigate the effect of varying vanadium doping levels on the properties of the ZnO nanorods. For CdS layer sensitisation on vanadium doped ZnO nanorods same silar process was performed.
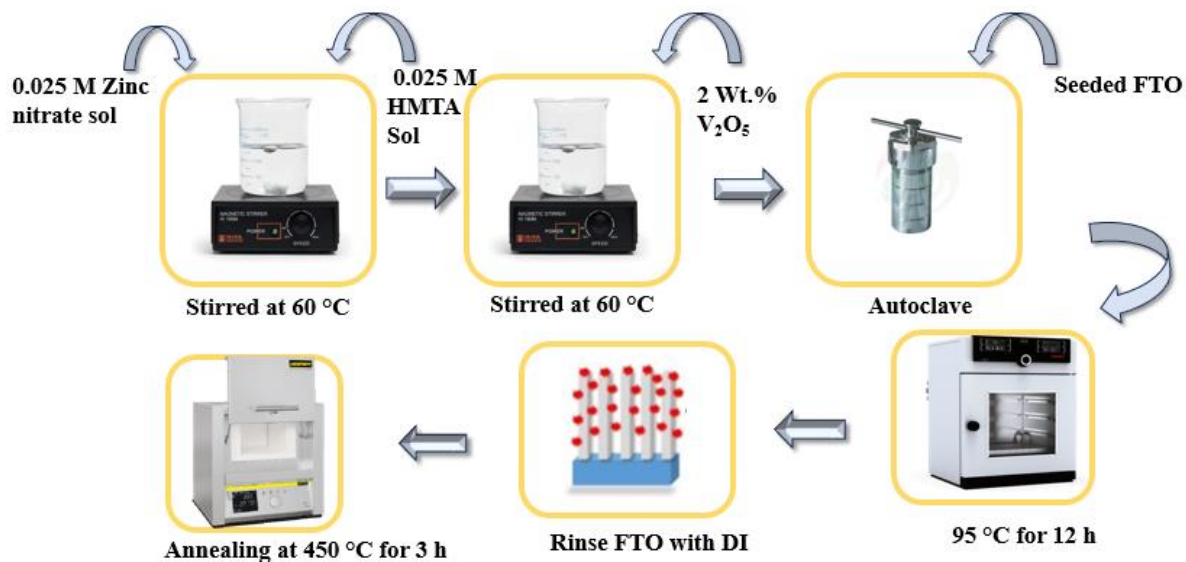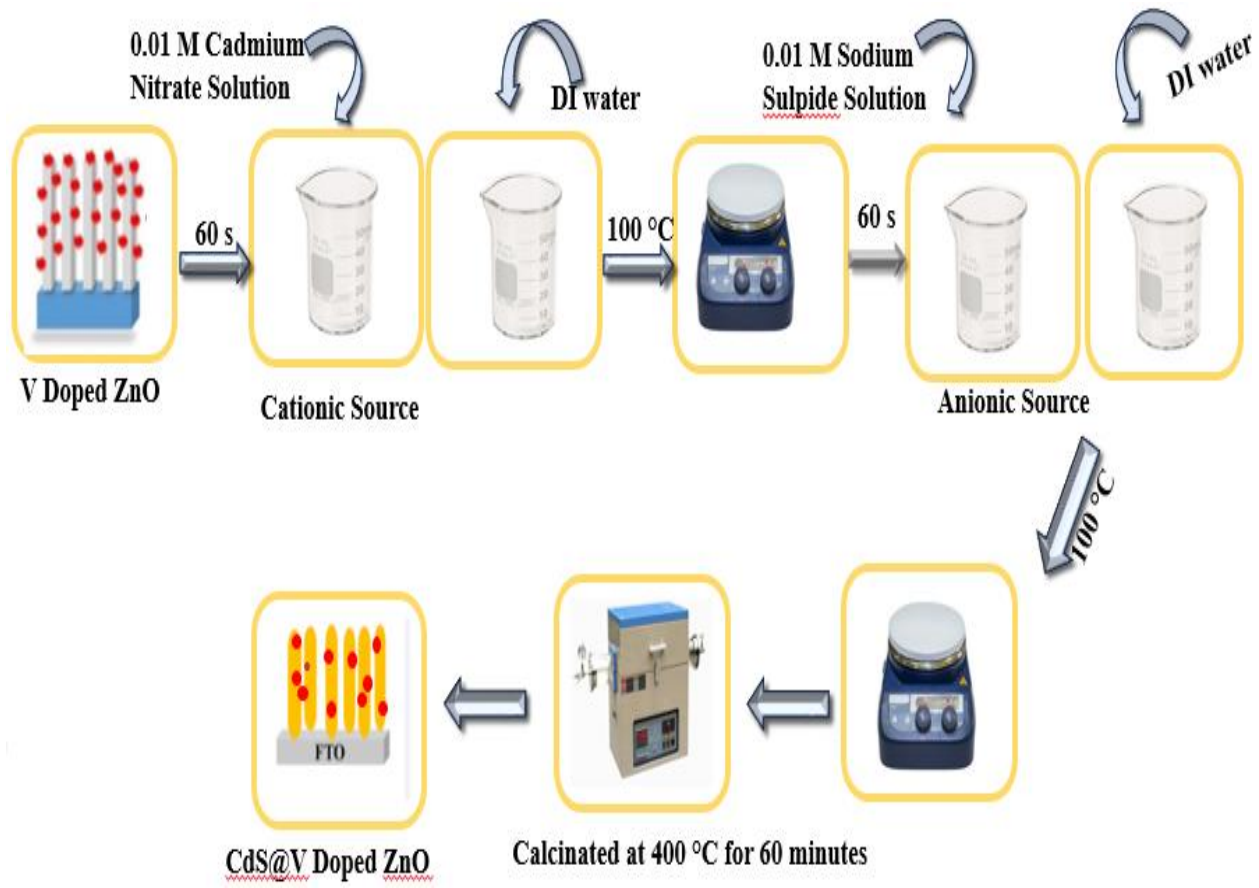

Figure 18: Vanadium doping on ZnO Nano rods

Figure 19: Synthesis of CdS@V doped ZnO

4. Results and discussions:

4.1. X-ray diffraction

Figure 20 shows the XRD pattern of synthesized 1D ZnO nanorods. All the diffraction peaks can be well indexed to hexagonal wurtzite-structured ZnO with three pronounced peaks(102), (002), and (101), appearing at $2\theta=47.8\circ$, $34.7\circ$, and $37.7\circ$, which match well with those of the standard ZnO XRD pattern (JCPDS 80-0074). No characteristic peakis observed for other impurities such as metallic Zn andZn(OH)2, indicating the purity of the products. The most intense peak at ~34.7°, indicating the preferred growth orientation along the c-axis. The crystallite size of all the materials were also calculated by using Dybe scherrer equation:
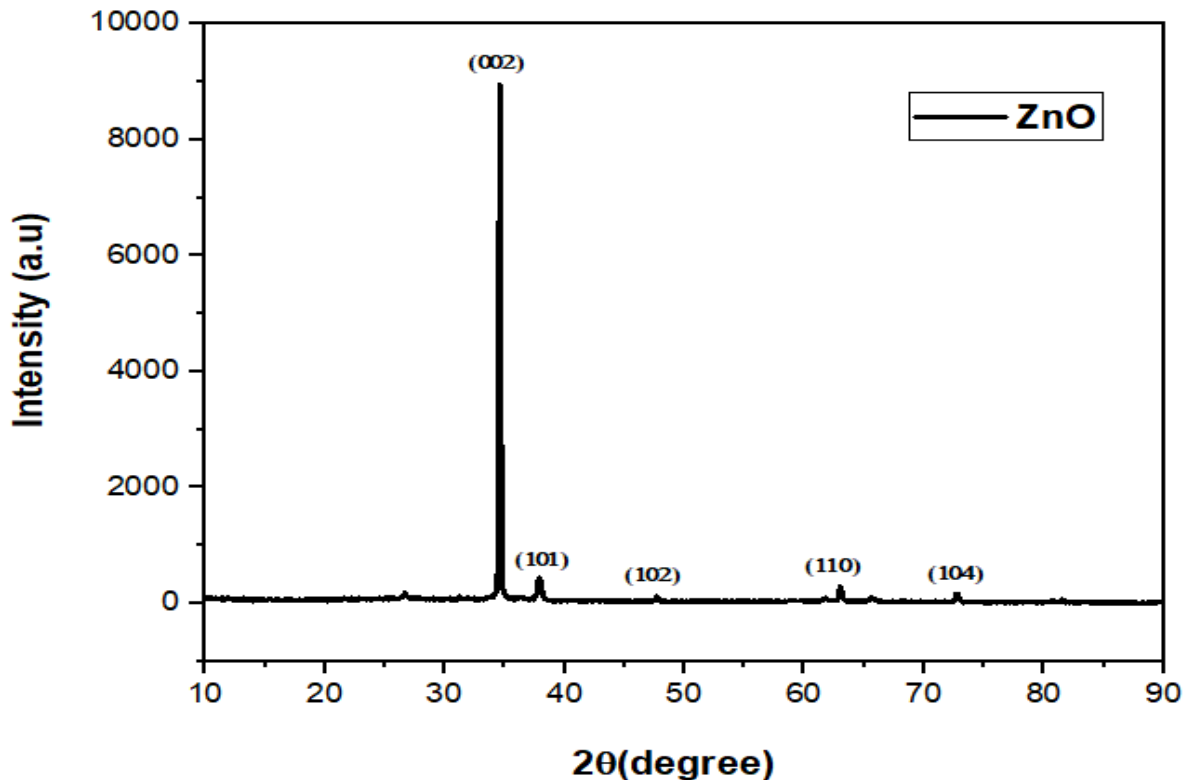
$$D = \frac{0.9\,\lambda}{\beta\cos\theta}$$

Figure 20: XRD of ZnO Nanorods

ZnO@CdS hetero-structures exhibited new diffraction peaks centered at°, 26.3°, 28.9°, 44.8°, 52.7°, corresponding to the crystal planes (111), (200),(220), (311), of the hexagonal phase of CdS

(JCPDS:80-0019) along with ZnO 1D peaks (shown in Fig.21). Increase in the intensity of 002 peak also confirms the hexagonal formation of CdS on 1D Zinc oxide.The result illustrated that ZnO@CdS nanorods 1D were composed of a hexagonal structure ZnO andCdS. Moreover, no crystal phase transformation of ZnO was observed after CdS coating, confirming that the obtained product was of high purity.
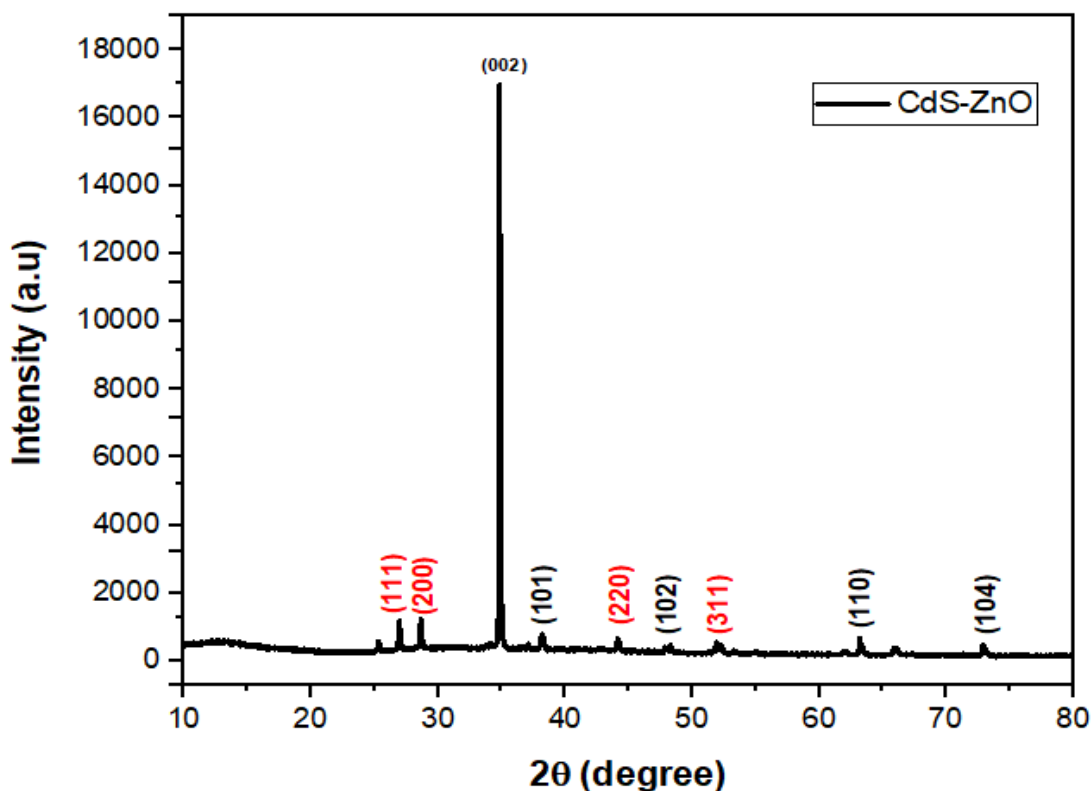

Figure 21: XRD of CdS-ZnO

Small shifts in ZnO peaks (such (002) was observed which shows successful doping of vanadium. vanadium doping also caused the formation of secondary phases observed at 29.3°, 55.3°, corresponding to the crystal planes (102), (110), (JCPDS:77-1757) along with other peaks(ZnO and CdS) (shown in Fig.22). Additional peaks shows formation of additional phase like V_2O_5 or $Zn_3V_2O_8$, it indicates solid solution formation of vanadium in the ZnO lattice. Small shifts in ZnO peaks (such (002) was observed which shows successful doping of vanadium. vanadium doping also caused the formation of secondary phases observed at 29.3°, 55.3°, corresponding to the crystal planes (102), (110), (JCPDS:77-1757) along with other peaks(ZnO and CdS) (shown in

Fig.22). Additional peaks shows formation of additional phase like V_2O_5 or $Zn_3V_2O_8$, it indicates solid solution formation of vanadium in the ZnO lattice.
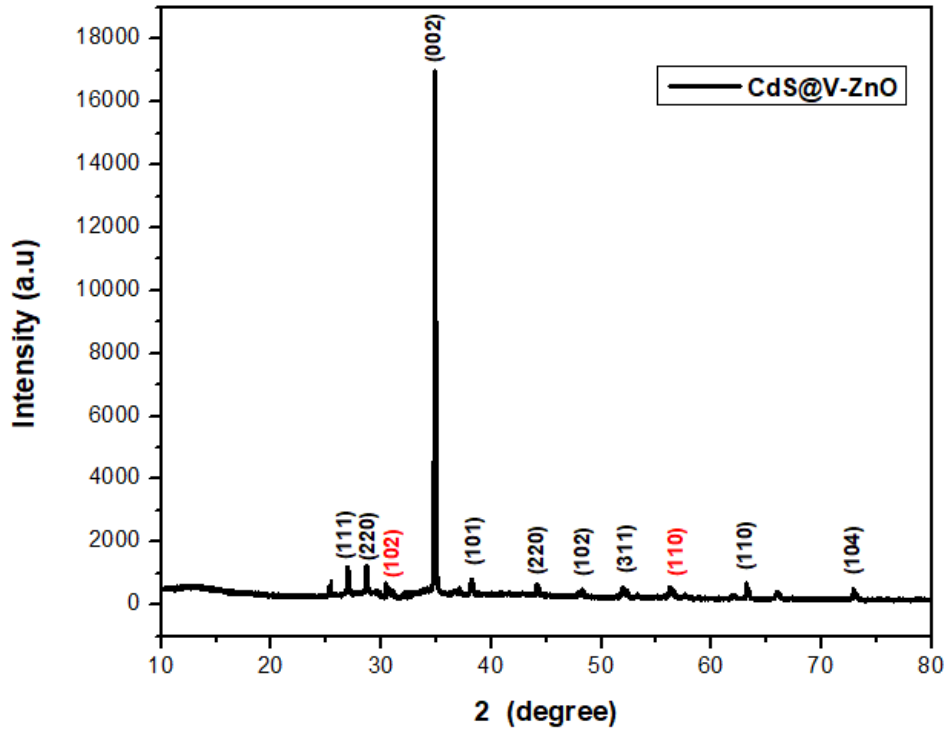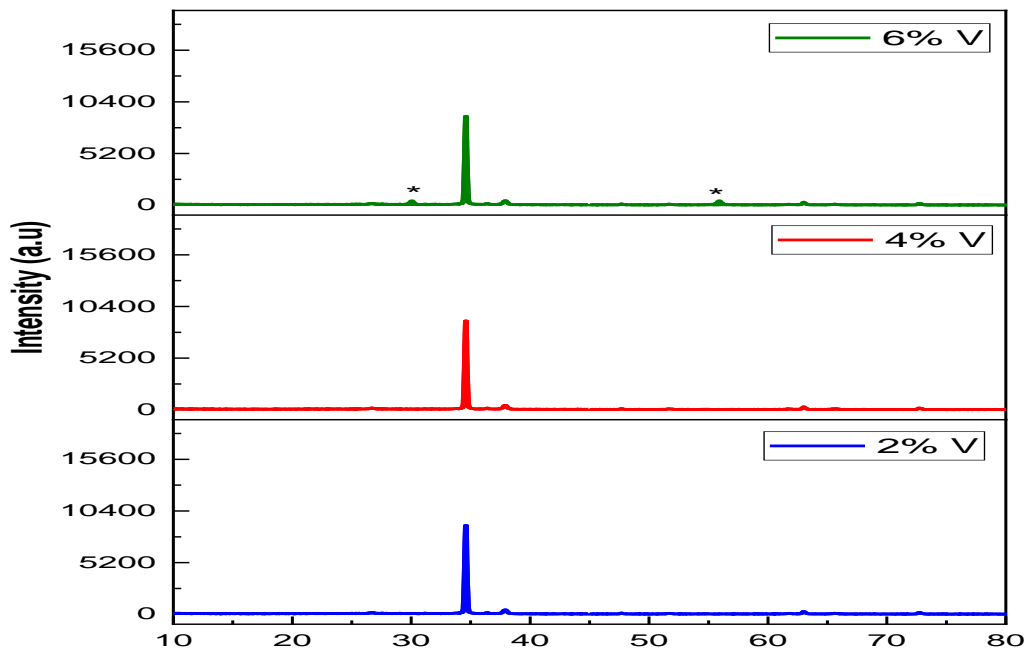

Figure 22: XRD of CdS@V-ZnO nano rods

Figure 23: Comparison of XRD between 2%, 4% and 6% V doping on ZnO nanorods

4.2. Raman Spectroscopy

The dominant peak in the Raman spectrum of ZnO typically appears around 520 cm⁻¹, corresponding to the E2 high mode. The intensity of this peak can be used to assess the crystal quality of ZnO nano rods, with sharper, more intense peaks indicating higher crystallinity. These peaks, found around 437 cm⁻¹ and 577 cm⁻¹, are linked to longitudinal optical phonons. The E1LO mode is associated with the zinc sub lattice, while A1LO corresponds to the oxygen sub lattice. Raman peaks around 200 cm⁻¹ are typically attributed to the E2 low phonon mode, which is usually weaker than other peaks. These peaks offer information on the crystal symmetry and the presence of defects in the ZnO nanorods. Shifts or broadening of the Raman peaks can reveal stress, strain, or doping effects in ZnO nanorods.
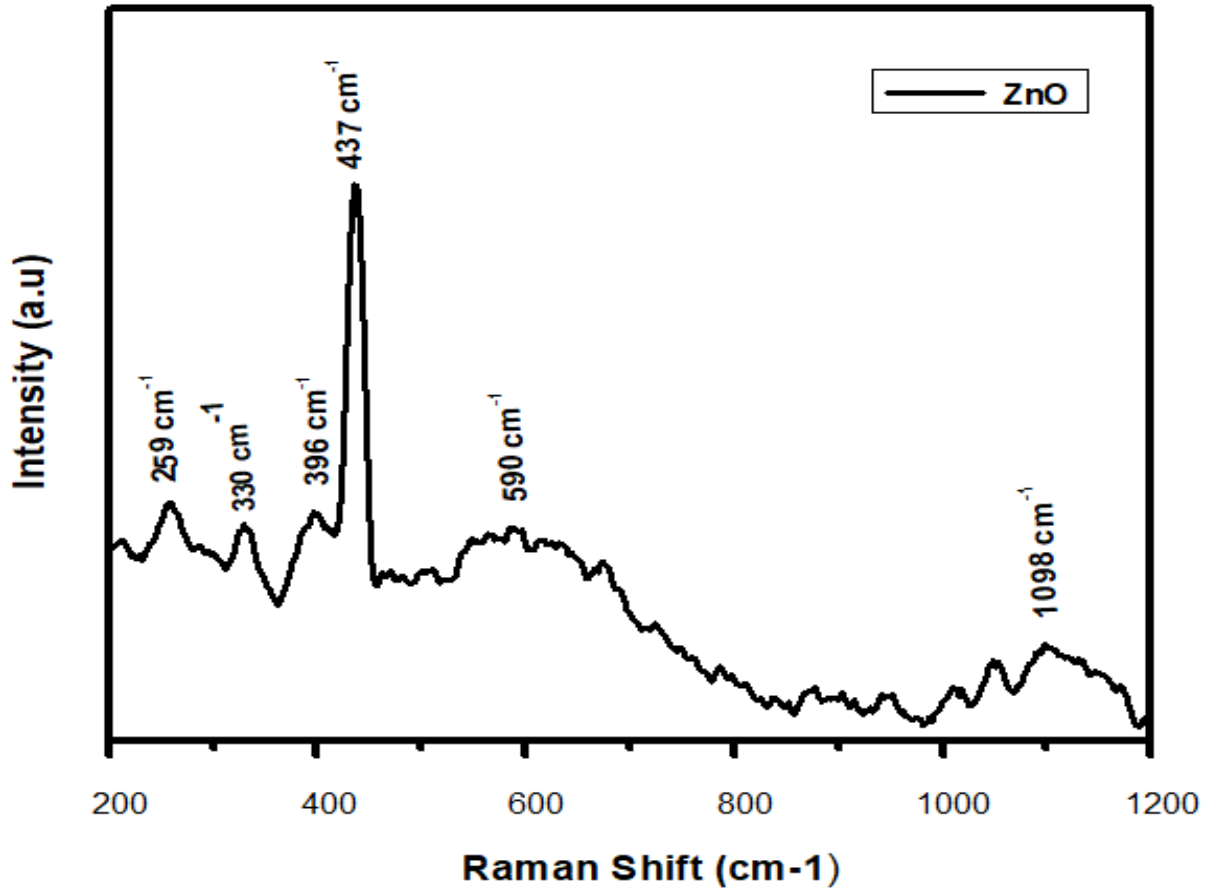

Figure 23: Raman of ZnO nano rods

CdS shows distinct Raman peaks in the 300–350 cm⁻¹ range, primarily linked to the E2 (high) and A1 vibrational modes in the CdS crystal structure. The peak around 300 cm⁻¹ corresponds to the

symmetric stretching vibration of the Cd-S bond (A1 mode), while the peak near 350 cm⁻¹ is related to the E2 mode, which involves the vibration of sulfur atoms in the lattice. These peaks confirm the presence of the CdS phase in the nanorods and offer insights into the crystalline quality of the CdS material.
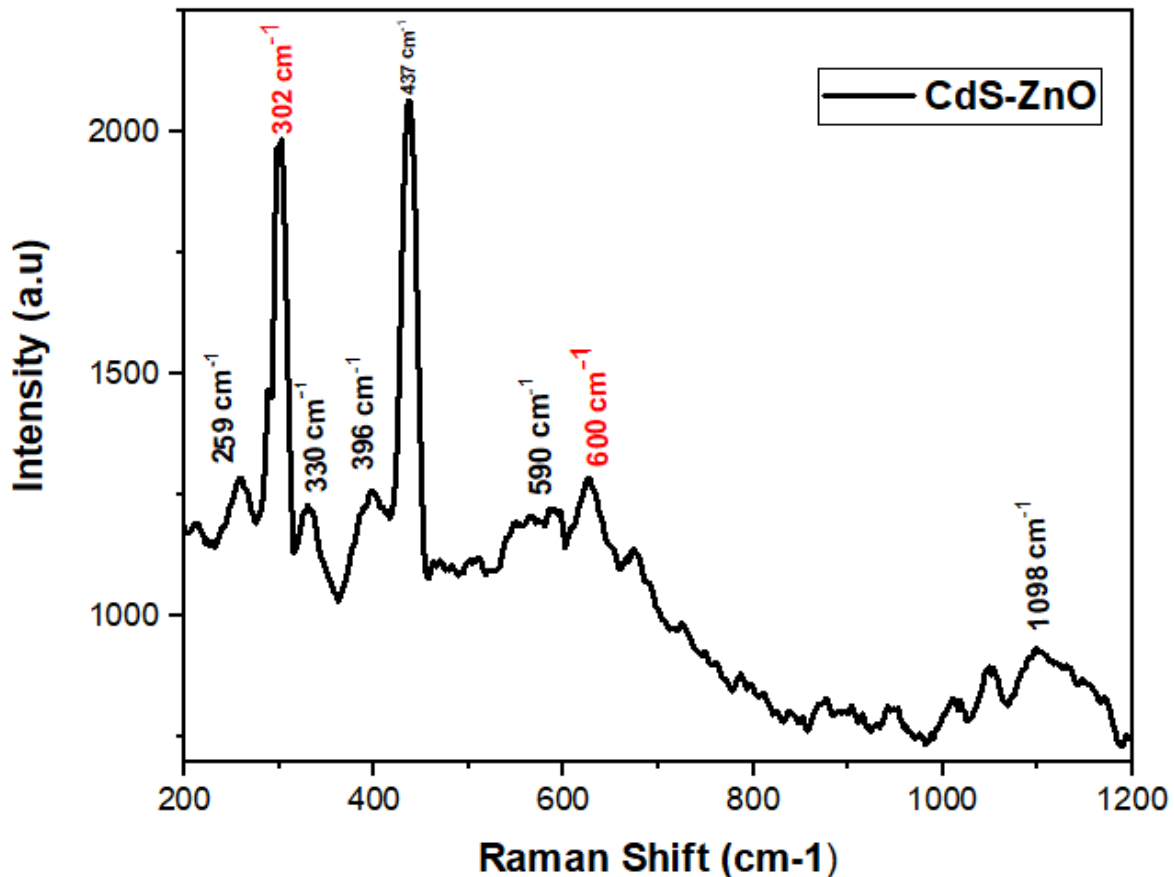

Figure 24: Raman of CdS-ZnO nano rods

Vanadium doping in ZnO can alter electron-phonon interactions, potentially leading to shifts in the positions of the ZnO Raman peaks, especially the E2 high mode. It can also cause the peaks to broaden due to the creation of additional electronic states within the ZnO band structure, affecting the material's vibrational modes. The degree of these shifts and broadening depends on the vanadium doping concentration.

Vanadium doping can also introduce defect-related peaks, typically observed in the 730 cm⁻¹ to 1000 cm⁻¹ range. These peaks are associated with oxygen vacancies, zinc interstitials, or defects

induced by vanadium. The presence of these peaks indicates structural disorder or nonstoichiometry in the nanorods, which plays a critical role in their electronic and photocatalytic properties
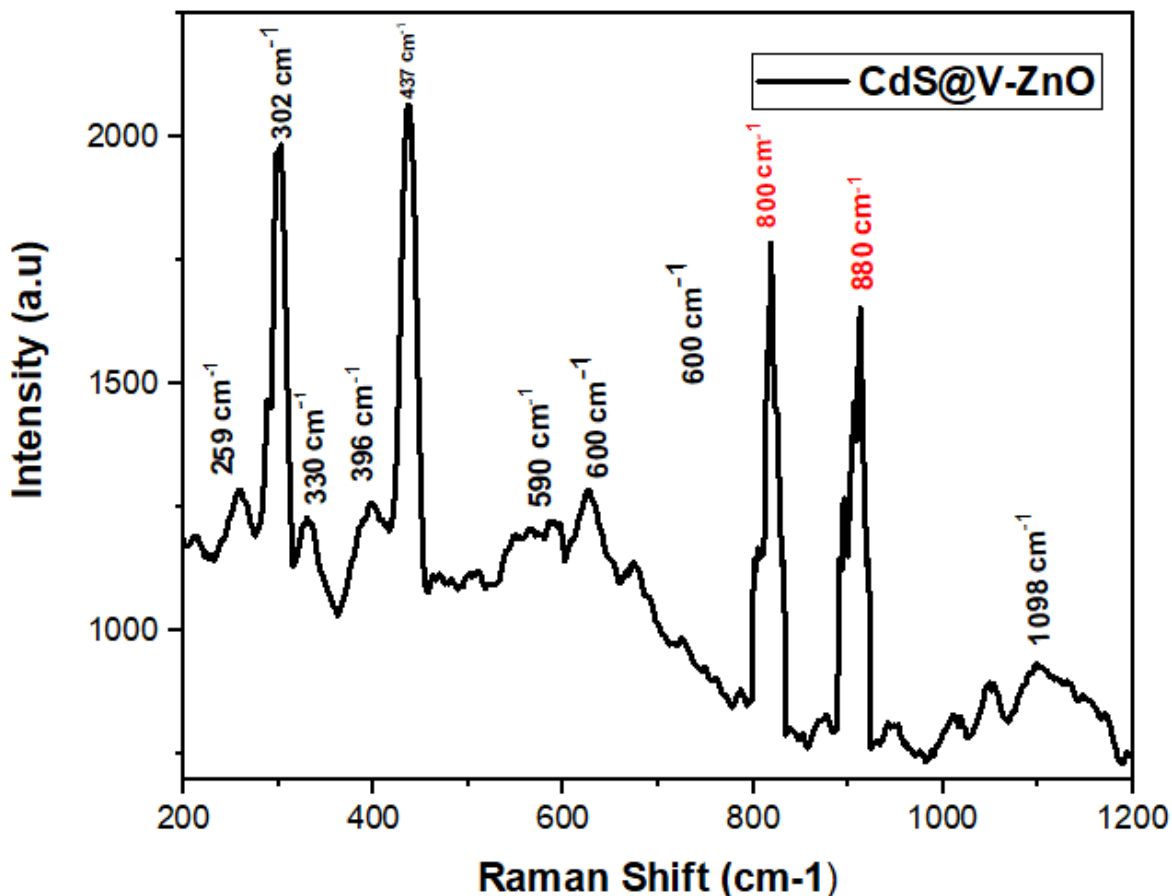

Figure 25: Raman of CdS@vdopedZnO

4.3. SEM analysis

One of the key characteristics of 1D ZnO nanorods is their rod-like structure. SEM images typically show long, straight, cylindrical nanorods with pointed tips, depending on the synthesis method. These nanorods generally have uniform diameter and length, though some variations can arise based on the conditions used during synthesis.The surface texture of ZnO nanorods can vary, with surfaces being either smooth or rough depending on the synthesis technique and conditions. For example, nanorods produced by hydrothermal synthesis tend to have smoother surfaces, while those made by methods like chemical vapor deposition (CVD) or sol-gel may exhibit rougher

surfaces due to residual particles or byproducts. SEM images might also reveal the presence of clusters or aggregates of nanorods. These can occur due to inadequate dispersion during synthesis or the close proximity of multiple growing nanorods. Aggregation can impact the material's performance in applications such as sensors or photocatalysis, where a high surface area is crucial. SEM can reveal the growth direction of the nanorods, which is typically along the [001] crystallographic axis in ZnO. The orientation of the nanorods is an important factor that affects their optical and electrical properties, as well as how they interact with light and other molecules, making it a critical consideration in material design.
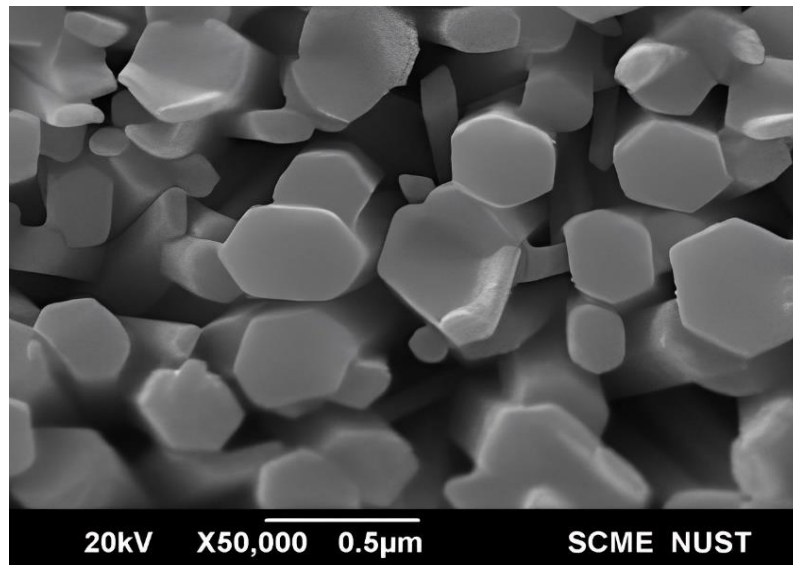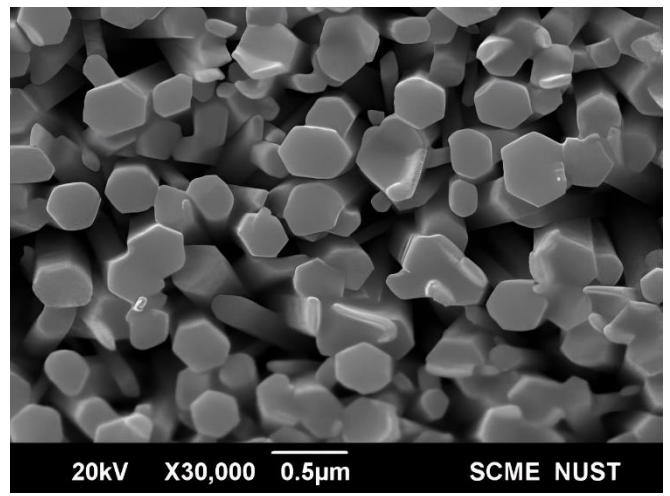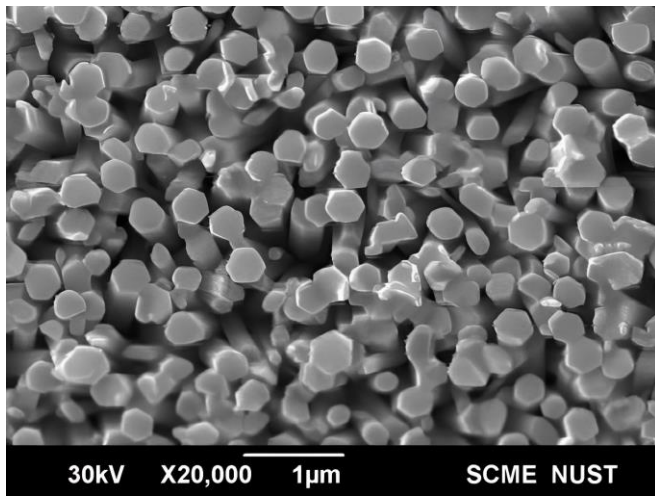

Figure 26: SEM analysis of CdS@VdopedZnO

5. Applications

5.1. **LSV**:

The photo response of all the samples was observed by measuring photocurrent density (J-V) characteristic peaks in the light illumination from -0.50 to 0.6V vs. Ag/AgCl. The onset potential values are also very important when dealing with photocatalysts. The 8 coat CdS@Vanadiumwt6% doped ZnO nanorods has the lowest onset potential than all other samples. The lowest onset potential indicates that photocatalysts can start its activity at lower energy input and have broad visible light absorption spectrum leads to higher efficiency. The photocatalyst which has the lowest onset potential shows the highest photocurrent density. The J-V curves of all photocatalysts in dark and light are shown in fig 27. Aaj to voting of CDS is increased on zinc oxide nano roads the photo current density is also increased and till the eight Coat. It is also observe that by increasing doping concentration from 2 to 6% vanadium photocutrent density is also increased from 30 to 220 microA/cm2 at 0.5 V versus Ag/AgCl. The increase in photocurrent density in 6%wt V doped is due to formation of extrinsic defects and oxygen vacancies. The extrinsic defects under conduction band (CB) of ZnO act as electron trapping sites and restrict the electrons to recombine with holes and increase the charge carries mobility. The oxygen vacancies help to increase the surface area of the photocatalyst leads to increase the active sites.
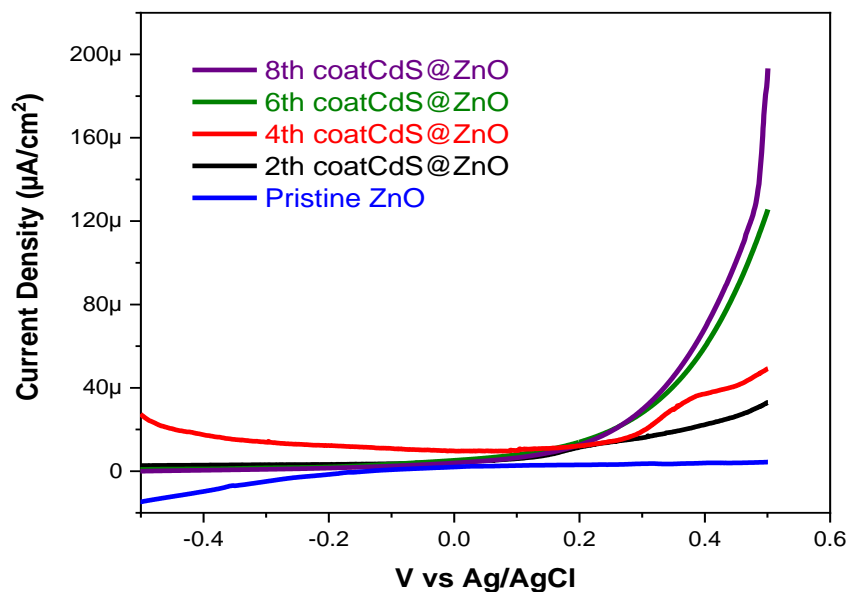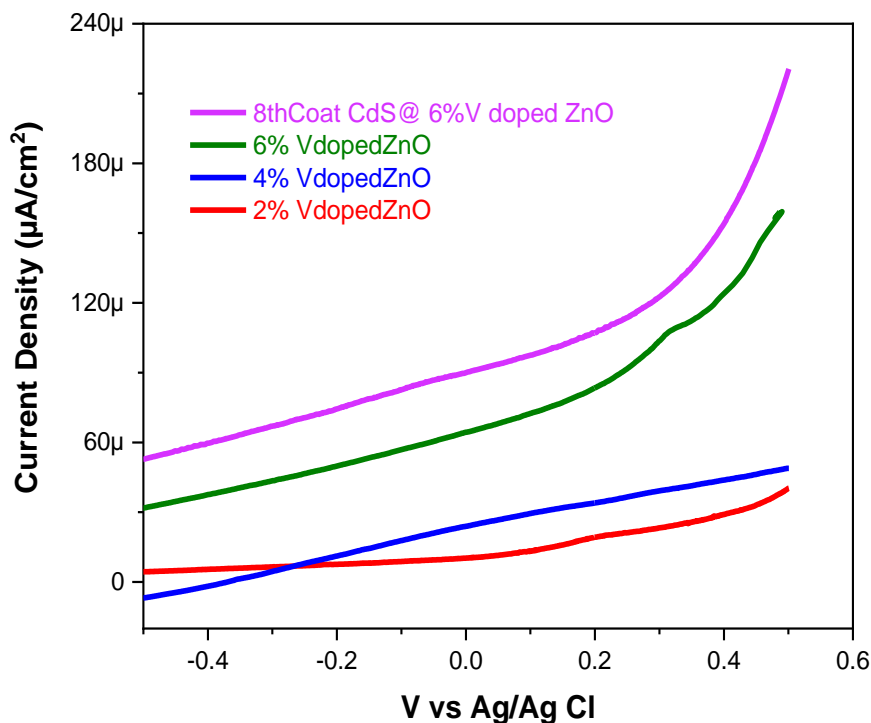
Figure 27: LSV

5.2. **Chronoanoamperometry**

In the figure 28, chopping curves of all the samples are recorded to study the photostability and photosensitivity of the photocatalyst for 1000 seconds(s) and by chopping the light in every few seconds. It is observed that for TiO2 and Bi2S3@TiO2 the photocurrent density is almost stable but with much less slope. The trend of photocurrent density follows in the same way as in the chopping curves. For for the cds sensitized zinc oxide the photo current density is increased as the number of coatings of cadmium sulphide are increased.

It is also been observe that 2% and 4% vanadium doped zinc oxide showed less photo current density as compared to 6% vanadium doped zinc oxide. The 8 coat CdS@Vanadiumwt6% doped ZnO shows stable and the highest photocurrent density curves throughout whole 1000s as compared to all samples. The 8 coat CdS@6% V doped ZnO shows the most stable and the highest photocurrent density because as vanadium doping increases the electron trapping sitesincrease that eventually leads to traps the electrons of CB of ZnO to avoid the recombination with the holes of VB and improve the mobility of charge carriers. This indicates the improvement of interfacial

charge transfer between photocatalyst and electrolyte and better charge separation at metal and semiconductor interface.
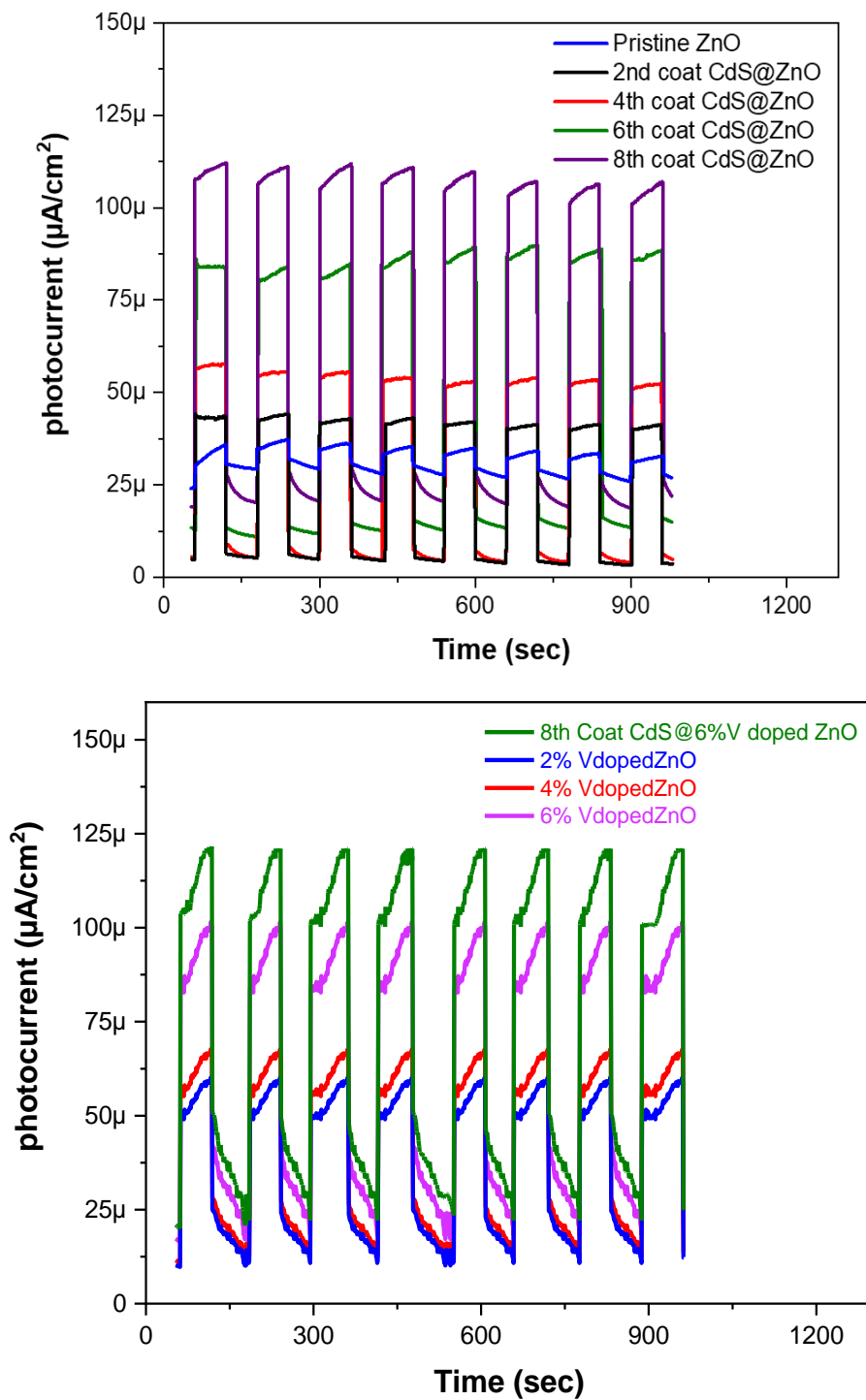

Figure 28: Chrono amperometry

5.3. **Electrochemical Impedance Spectroscopy**:

Nyquist Plot:

In order to get the deeper insight into charge carrier inject, resistance distribution, charge recombination and life time of charge carriers of the prepared photoanodes were measured by electrochemical impedance spectroscopy (EIS) in the light. The EIS experimental data was fitted into equivalent circuit model (fig 29) to identify charge carrier resistance and charge recombination where Rs is solution resistance, Rct is charge transfer resistance, Y0 and α are exponent and coefficient of CPE (constant phase element) and its value is n=0-1. CPE value depends on smooth surface of photoanode and zero indicates the lowest smoothness and one shows the highest smoothness of surface. While W indicates the Warburg impedance which is due to electrolyte diffusion at the surface of photoanode. Plot shows that the 8 coat CdS@6% V doped ZnO NRs has the lowest Rct values that is agreed with LSV values. In the light, Nyquist curves show only one semicircle with smaller radius for each photoelectrode is introduced which is charge transfer resistance at low frequency. It means the charge transfer resistance is prominent in the light. The photoanode 8 coat CdS@6% V doped ZnONRs has the smallest radius of impedance which means it has the highest charge transfer mobility and the lowest recombination rate.
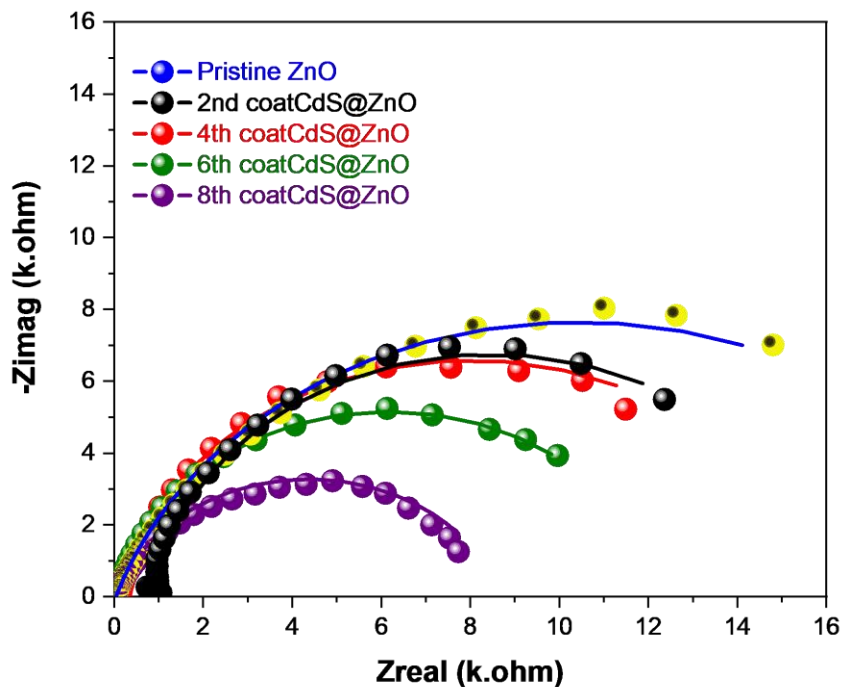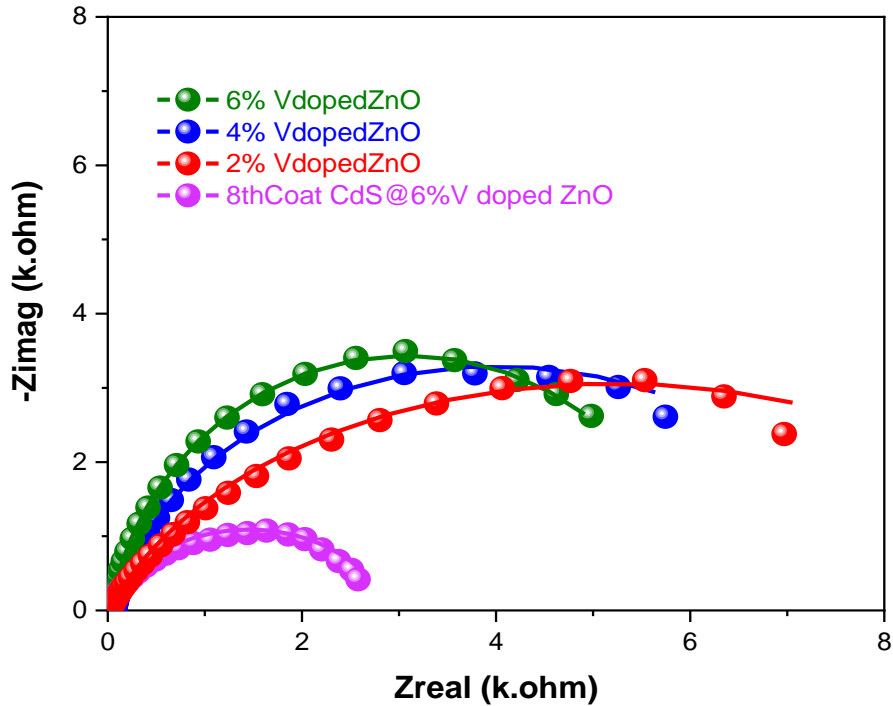
5.4. **Mott Schottky (M-S) curves**:

Mott Schottky curves are shown in fig30. The fig 30 shows that all the materials are n-type because all the materials show positive mott Schottky plots.

$$slope= 2/q\mathscr{E}0\mathscr{E}Nd$$

where q is electron charge, $\mathscr{E}0$ is dielectric constant, $\mathscr{E}$ is permittivity of the material and Nd is donor densities or carrier densities. From the equation, we know that slope is inversely proportional to donor densities. So from the plot, it can be concluded that by increasing the CDS sensitization on the zinc oxide, the value of donor densities will increase as the slopes become flatter with each layer. It can also be concluded that by increasing the doping level from 2 to 6 percent weight vanadium onto the zinc oxide, the slope becomes flatter and flatter, and donor densities value increases. 8-coat CdS on vanadium6wt%-doped zinc oxide showed the highest value for donor density and the flattest slope. The increase in the donor densities is due to introduction of extrinsic defects, splitted molecular orbitals and oxygen vacancies due to introduction of vanadium ions as a dopant. The extrinsic defects and oxygen vacancies act as hole trapping sites for holes of

CdS and do not allow them to recombine with electrons of doped ZnO NRs. These holes are further quenched by sacrificial agents and oxidation of quenching material takes place. These factors cause to enhance the donor densities values of the material upon doping.
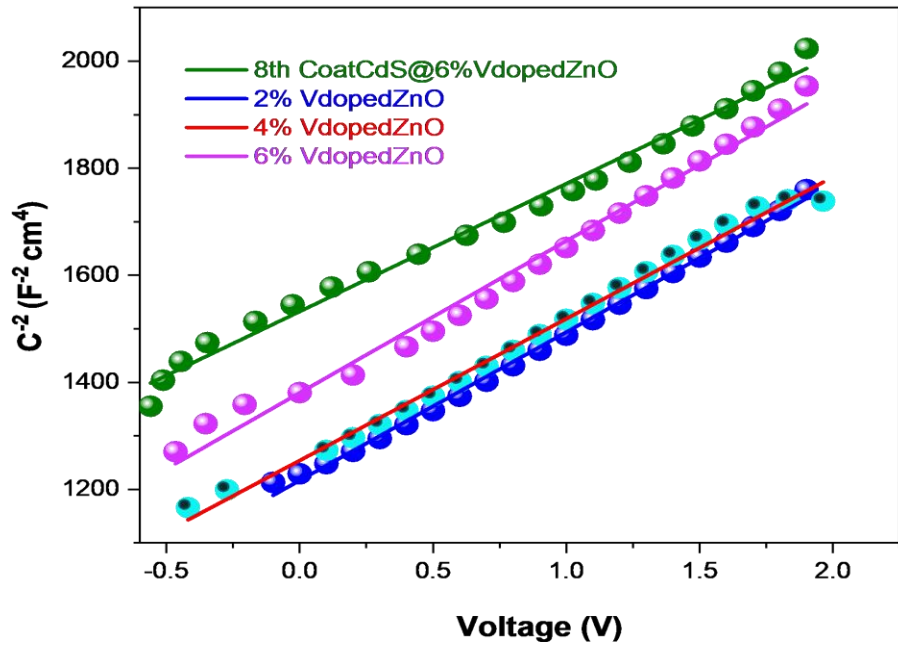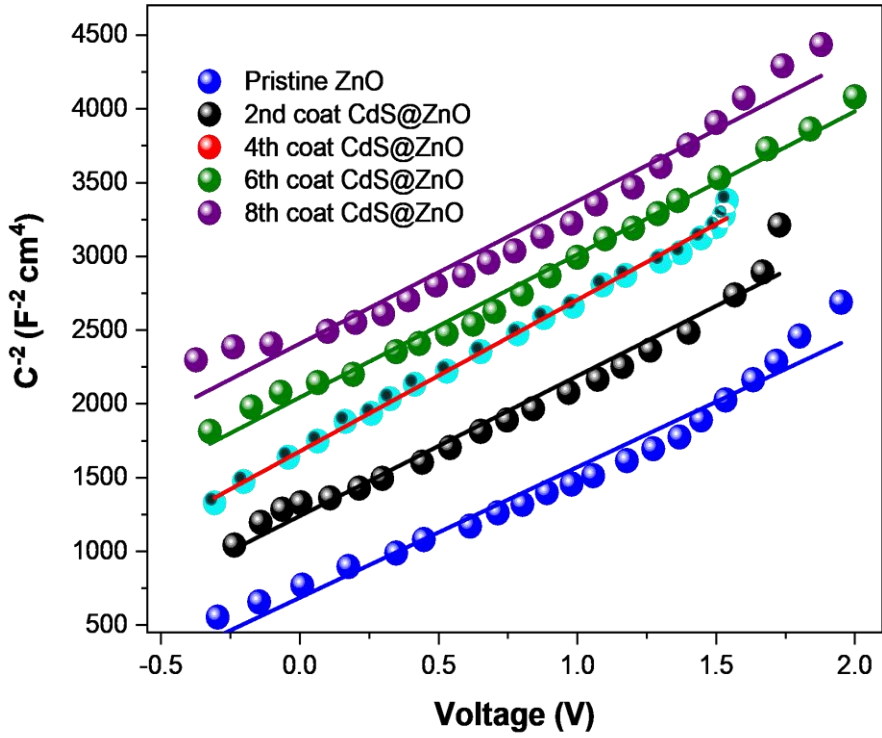

Figure 30: Mott Shottkty

Chapter 5

5.1. Conclusions

A novel core shell CdS@vdoped ZnO NRs heterostructure was synthesized and characterized successfully for photoelectrochemical hydrogen production. 8 cycled CdS was optimized on NRs with photocurrent density values 0.06 mA/cm^2. It shows the lowest charge transfer resistance, band gap values and the highest photoconversion efficiency values. After doping with V ions, the photocurrents density values and photoconversion efficiency values started to increase and charge transfer resistance goes to decrease. The photocatalyst CdS@vdoped ZnO NRs shows the highest photocurrent density values 0.51 mA/cm^2 and the lowest charge transfer resistance values 5.724 kΩ in the light. It shows the highest photoconversion efficiency value 0.24% vs RHE. This shows the successful type-II heterojunction formation which increase the charge carrier transfer and reduces the charge recombination by making Schottky barrier between them.

References

1. Mohammadi, A. and M. Mehrpooya, *A comprehensive review on coupling different types of electrolyzer to renewable energy sources.* Energy, 2018. **158**: p. 632-655.

2. Lu, Y., et al., *A critical review of sustainable energy policies for the promotion of renewable energy sources.* Sustainability, 2020. **12**(12): p. 5078.

3. Marks-Bielska, R., et al., *The importance of renewable energy sources in Poland's energy mix.* Energies, 2020. **13**(18): p. 4624.

4. Yılmaz, A.O. and T. Uslu, *The role of coal in energy production—Consumption and sustainable development of Turkey.* Energy Policy, 2007. **35**(2): p. 1117-1128.

5. Li, X.-S., et al., *Investigation into gas production from natural gas hydrate: A review.* Applied Energy, 2016. **172**: p. 286-322.

6. Kutcherov, V.G., V.V. Bessel, and A.S. Lopatin, *The paradigm shift in the global energy market: domination of natural gas.* Proceedings of the 17th International multidisciplinary scientific geoconference SGEM, 2017. **2017**: p. 813-820.

7. Yu, C., et al., *Impact of non-renewable energy and natural resources on economic recovery: Empirical evidence from selected developing economies.* Resources Policy, 2023. **80**: p. 103221.

8. Weiland, N., et al., *Fossil energy*, in *Fundamentals and Applications of Supercritical Carbon Dioxide (sCO₂) Based Power Cycles*. 2017, Elsevier. p. 293-338.

9. Foley, A.M., et al., *Current methods and advances in forecasting of wind power generation.* Renewable energy, 2012. **37**(1): p. 1-8.

10. Maika, N., W. Lin, and M. Khatamifar, *A Review of Gravitational Water Vortex Hydro Turbine Systems for Hydropower Generation.* Energies, 2023. **16**(14): p. 5394.

11. Wei, L., et al., *The effect of precipitation on hydropower generation capacity: a perspective of climate change.* Frontiers in Earth Science, 2020. **8**: p. 268.

12. Kannan, N. and D. Vakeesan, *Solar energy for future world:-A review.* Renewable and sustainable energy reviews, 2016. **62**: p. 1092-1105.

13. Guangul, F.M. and G.T. Chala. *Solar energy as renewable energy source: SWOT analysis*. in *2019 4th MEC international conference on big data and smart city (ICBDSC)*. 2019. IEEE.

14. Mekhilef, S., R. Saidur, and A. Safari, *A review on solar energy use in industries.* Renewable and sustainable energy reviews, 2011. **15**(4): p. 1777-1790.

15. Balat, M. and G. Ayar, *Biomass energy in the world, use of biomass and potential trends.* Energy sources, 2005. **27**(10): p. 931-940.

16. Rosillo-Calle, F., *A review of biomass energy–shortcomings and concerns.* Journal of Chemical Technology & Biotechnology, 2016. **91**(7): p. 1933-1945.

17. Wang, L., et al., *Design, modification and application of semiconductor photocatalysts.* Journal of the Taiwan Institute of Chemical Engineers, 2018. **93**: p. 590-602.

18. Elumalai, N.K., et al., *Metal oxide semiconducting interfacial layers for photovoltaic and photocatalytic applications.* Materials for Renewable and Sustainable Energy, 2015. **4**: p. 1-25.

19. Wang, Z., et al., *Recent developments in p-Type oxide semiconductor materials and devices.* Advanced Materials, 2016. **28**(20): p. 3831-3892.

20. Sumikura, S., et al., *Photoelectrochemical characteristics of cells with dyed and undyed nanoporous p-type semiconductor CuO electrodes.* Journal of Photochemistry and Photobiology A: Chemistry, 2008. **194**(2-3): p. 143-147.

21. Low, J., et al., *Heterojunction photocatalysts.* Advanced materials, 2017. **29**(20): p. 1601694.

22. Jia, X., et al., *Transforming type-I to type-II heterostructure photocatalyst via energy band engineering: a case study of I-BiOCl/I-BiOBr.* Applied Catalysis B: Environmental, 2017. **204**: p. 505-514.

23. Zhang, L., et al., *Emerging S-scheme photocatalyst.* Advanced materials, 2022. **34**(11): p. 2107668.

24. Chen, W., et al., *Surface transfer doping of semiconductors.* Progress in Surface Science, 2009. **84**(9-10): p. 279-321.

25. Joy, J., J. Mathew, and S.C. George, *Nanomaterials for photoelectrochemical water splitting–review.* International Journal of hydrogen energy, 2018. **43**(10): p. 4804-4817.